

Characterizing subarctic biomes for land surface modeling of pollution and climate risk

Stefanie Falk¹, Ane V. Vollsnæs², Aud B. Eriksen², Lisa Emberson³, Connie O'Neill³, Frode Stordal¹, and Terje Koren Berntsen¹

¹Department of Geosciences, University of Oslo, Oslo, Norway

²Department of Biosciences, University of Oslo, Oslo, Norway

³Department of Environment and Geography, University of York, UK

Correspondence: Stefanie Falk (stefanie.falk@geo.uio.no)

Abstract. The unique vegetation of the subarctic region, acclimatized to extremes of cold and midnight sun, are likely to be at threat from the combined impacts of climate change and increasing ozone (O_3) concentrations. The atmospheric and climatic characteristics of the subarctic are known to lead to pronounced peak O_3 concentrations in spring. To date, only a few studies have been conducted to assess the response of subarctic vegetation to variations in climate and air pollution. This study looks

5 to fill this knowledge gap by examining trends in climate variables and O_3 concentrations that have occurred over the past few decades. These climatological and O_3 data are used to assess the extent to which two recent years (2018 and 2019) deviate from climatic and O_3 concentration norms and how these current (and potentially more frequent future) deviations may influence O_3 damage to subarctic vegetation. We find that 2018 was an anomalously warm and bright year (in particular in spring and early summer) with higher than average O_3 concentrations in April/May and a high number of episodic peak O_3 concentration above
10 40 ppb in June–August, the latter in part attributable to an increase in forest fires in the Northern Hemisphere as well as warmer and sunnier conditions. We apply a flux-metric (phytotoxic ozone dose, POD) to determine O_3 risk and damage to vegetation as a function of O_3 concentration, climate variables, and species-specific physiology. We find that bespoke parameterizations of plant functional types (PFTs) for subarctic vegetation bio-types increase estimates of ozone-induced biomassloss by 2.5 to 17.4 %. Our study, suggests that assessments that use generic parameterizations are likely to underestimate the risk of O_3
15 damage in this region. We conclude that appropriate parameterization for the growing season and plant physiological responses to light and temperature are particularly important for accurate modeling of seasonal gas exchange. Efforts should be targeted towards accurately defining subarctic ecotype physiological response of PFTs to climatic variables to improve regional and global scale biogeochemical cycling under current and future climates.

1 Introduction

20 Ground-level ozone (O_3) is a highly toxic pollutant known to cause damage to human health (WHO - World Health Organization, 2008) and to a variety of ecosystems around the World (Emberson, 2020). Ozone is a cause of visible injury, photosynthetic damage, early senescence as well as programmed cell death of plants (Kangaskärvi et al., 2005). Annual global yield losses of four major crops (wheat, rice, maize, and soybean) of 3 – 15 % (Ainsworth, 2017) and a suggested loss in pri-

mary production in forestry of 7% (Wittig et al., 2009; Matyssek et al., 2012) has been attributed to ozone. The crop yield loss studies indicate a threat to food security in rapidly developing countries, e.g., in East and South-East Asia (Tang et al., 2013; Tai et al., 2014; Chuwah et al., 2015; Mills et al., 2018), where ozone concentrations related to enhanced pollutant emissions from the transport, residential, power generation, and industrial sectors have increased in the past few decades. Even though long-term (pre-1950) observations of ground-level ozone concentrations are scarce; evidence from trend analysis of those few sites suggests that since the industrial revolution, background concentrations in the northern hemisphere have at least doubled and continued to increase (IPCC - Intergovernmental Panel on Climate Change, 2013, Chapter 2). Recent trend analyses for Europe indicate that a maximum was reached in 2007 (Derwent et al., 2018), after which tropospheric ozone started to level off or even decline (Cooper et al., 2014; Wespes et al., 2018; Gaudel et al., 2018). This can be attributed to a successful implementation of air quality regulations coupled with economic restructuring, reducing the number of episodes of peak concentrations especially in summertime over Europe and North America (e.g., Fleming et al., 2018; Mills et al., 2018). However, changes in environmental conditions associated with climate change, such as an increase in the frequency of heatwaves, could negate the effectiveness of emission reductions in relation to ozone impacts and air quality (Lin et al., 2020).

Complex photochemical cycles involving precursor gases such as carbon monoxide (CO) and hydrocarbons known as volatile organic compounds (VOCs) in the presence of nitrogen oxides (NO_x) lead to the formation of O_3 at ground-level. Despite a relatively short average tropospheric lifetime of approximately 22 days, ranging from a few days in the tropical boundary layer to up to 1 year in the upper troposphere (Stevenson et al., 2005; Young et al., 2013), ozone and its precursors are subject to advection over long distances. Episodes of high ozone concentrations in the absence of local pollution sources can therefore often be attributed to the long-range transport of both ozone and its precursors. In northern Fennoscandia, episodes of enhanced ozone concentrations in 2003 and 2006 have been traced back to ozone precursor emissions related to forest fires in southern and eastern Europe, respectively (Lindskog et al., 2007; Karlsson et al., 2013). Besides VOCs from anthropogenic sources, hydrocarbons are also emitted by vegetation itself in the form of terpenes and monoterpenes, so-called biogenic volatile substances (BVOCs). These emissions are thought to be a response to factors, such as thermal stress, defense against herbivores, or even attraction of pollinators (Peñuelas and Llusia, 2003).

In the annual cycle in Boreal climates, a distinct maximum of ground-level ozone concentrations typically occurs in spring followed by lower concentrations throughout the summer. Several conditions unique to the Arctic are stimulating the formation of this spring peak. Major pathways of ozone and its precursors' removal from the boundary layer include dry deposition on vegetated surfaces and photochemistry (Clifton et al., 2020). As dry deposition to bare ground or snow and ice-covered surfaces was found to be low (Helmig et al., 2007), both pathways of removal are substantially suppressed during polar night (Monks, 2000). This leads to a build-up of ozone and its precursors during winter. Come spring precursors are photochemically activated again, while snow cover typically continues to prevail and suppress ozone dry deposition. On the other hand, very high ozone concentrations occurring over shorter periods can often be attributed to deep tropopause folding events over the Arctic during winter. These events facilitate an intrusion of stratospheric air masses which are enriched in ozone (Škerlak et al., 2015). The spring peak is more pronounced in northern Fennoscandia than in more southern locations but shows a high interannual variability (Klingberg et al., 2009, 2019). A cause for this is the complex interplay between atmospheric dynamics

and chemistry (Laurila and Hakola, 1996; Hatakka et al., 2003) as described above as well as anthropogenic and biogenic activity (Rummukainen et al., 1996; Simpson et al., 2002; Galbally and Roy, 2007; Schnell et al., 2009). Andersson et al. (2017) showed in a modeling study focused on Fennoscandia that the variability of ozone concentrations in winter can be attributed mainly to changes in atmospheric background (transport) of ozone, while summertime abundance is mostly affected by emissions of precursors in the rest of Europe. Meteorology plays an important role throughout the year.

The start of the growing season (GS) in northern Fennoscandia has been shifting to earlier dates in response to the general warming trend (Menzel et al., 2006; Høgda et al., 2013; Karlsen et al., 2007, e.g.) and thereby converging with the period of the ozone spring peak. At the same time, the growing season is also becoming longer. A longer growing season is prolonging the time in which vegetation can accumulate ozone. For natural and semi-natural vegetation which is already subject to rapid climatic changes known as Arctic amplification (AMAP - Arctic Monitoring and Assessment Programme, 2012; IPCC - Intergovernmental Panel on Climate Change, 2013), these factors could promote a higher potential risk for northern vegetation to ozone-induced damage in the not so distant future.

Ozone acts as oxidative stress to plants. Its main action is imposed through reactions occurring in the cell walls and cell membranes of mesophyll cells inside the leaves. Ozone enters the leaves through stomata, leaf pores that enable gas exchange, allowing the entry of CO₂ for photosynthesis and loss of H₂O vapor via the plant transpiration stream. Stomatal aperture, and hence stomatal conductance to these gases (including ozone) will vary over the day and growing season primarily to balance CO₂ uptake against H₂O vapor loss. The higher the stomatal conductance, the higher the potential for ozone uptake. Stomatal conductance has been empirically linked to environmental factors such as air temperature *T*, photosynthetic photon flux density (PPFD), vapor pressure deficit (VPD), and soil water potential (SWP) as well as photosynthesis itself (Jarvis, 1976; Ball et al., 1987; Emberson et al., 2000; Mills et al., 2017, e.g.). Results from open-top chamber (OTC) experiments on downy birch (*Betula pubescens*) and mountain birch (*Betula pubescens toruosa*), native to subarctic regions, indicated reductions in both biomass, in root:shoot ratio, and visible leaf damage under elevated ozone treatment ($\langle [O_3] \rangle = 36 - 54 \text{ ppb}$) (Manninen et al., 2009). Although Scots pine (*Pinus sylvestris*) is considered to be more ozone tolerant due to an absence of visible injuries (Girgždienė et al., 2009), Manninen et al. (2009) found chlorophyll:carotenoid ratio and polyamines reductions under elevated ozone concentrations indicating susceptibility to ozone also in these species.

A substantial body of evidence exists that suggests flux-based metrics, that relate stomatal ozone uptake to vegetation damage, are biologically more relevant for risk assessments than exposure-based metrics. This is because they can account for particular species characteristics (i.e. physiology and phenology) as well as environmental conditions that can decouple the relationship between ozone concentration, ozone uptake, and consequent damage (Emberson, 2020). These flux-based metrics are better suited to represent the actual risk to vegetation from ozone, especially in the climatically extreme parts of Europe (Simpson et al., 2007; Mills et al., 2011, 2017). Most of these previous studies have focused on the Mediterranean where soil moisture deficits are thought to be most influential in decoupling concentration from uptake. Relatively few studies have explored the situation in Northern European climates where low temperatures may be considered more likely to influence ozone uptake (Juran et al., 2018, e.g.).

To estimate the flux-based metric, also referred to as the Phyto-toxic Ozone Dose over a threshold y (POD_y), an estimate 95 of the stomatal O_3 flux (Φ_{sto}) is calculated based on the assumption that the concentration of O_3 at the top of the canopy represents a reasonable estimate of the concentration at the upper surface of the laminar layer for a sunlit upper canopy leaf and environmental factors affecting stomatal conductance as described further in Section 4. POD_y is then calculated according to:

$$POD_y = \int (\Phi_{sto} - y) \cdot dt, \quad (1)$$

with the hourly averaged stomatal ozone flux Φ_{sto} (see Eq. (B6)) and a stomatal ozone flux threshold y both given in units of 100 $nmol\ O_3\ m^{-2}\ PLA\ s^{-1}$. The flux threshold y represents the detoxification potential of the plant and is typically only exceeded during daylight hours (i.e. when global radiation is above $50\ W\ m^{-2}$). POD_y is given in $mmol\ m^{-2}$ over the growing season.

The POD_y metric is currently used in risk assessments under the United Nations Economic Commission for Europe (UNECE) Long Range Transboundary Air Pollution (LRTAP) Convention to identify those locations across Europe where vegetation is at risk from ozone. This convention aims to develop an effects-based emission reduction policy that can target those 105 ozone precursor emissions that are most influential in causing damage. To achieve this the concept of critical levels (CLs) has been developed and applied (Maas et al., 2016). Exceedance of the CL is used to identify those areas across Europe that would benefit from targeted Europe-wide emission reductions. Methods to estimate POD_y and CLs are defined by the UNECE LRTAP Convention and described in a Mapping Manual (Mills et al., 2017). The CL is calculated by:

$$CL_{exceed} = POD_y - CL. \quad (2)$$

An application of the Mapping Manual method was made by Mills et al. (2011) where exceedance of the CL was related to 110 observations of ozone damage to a clover bio-monitor. This study demonstrated the improved ability of flux-based metrics (in comparison to exposure-based metrics) to identify the geographical distribution of the risk of ozone damage and also showed that the ozone damage could extend into more northerly regions of Europe. A similar bio-monitoring study was conducted at the Norwegian Institute of Bioeconomy Research (NIBIO) Environment Centre Svanhovd to assess whether local ozone 115 concentrations were capable of inducing damage to vegetation growing under northern Fennoscandia conditions. In 2018, we indeed observed ozone damage on clover and tobacco. In contrast, no such damage was found on the clovers in 2019.

According to a report by the Norwegian Meteorological institute (Gangstø Skaland et al., 2019), the summer of 2018 was the warmest and driest ever recorded in eastern, western, and southern Norway. In the north (including Finnmark), it was amongst the warmest on record – favorable conditions for ground-level ozone formation. An unusually weak and northward shifted 120 jet stream allowed for a persistent high-pressure system above northern Europe, including Fennoscandia which blocked the low-pressure systems for several consecutive months. In the period May – July, southern Norway had temperatures $4\ ^\circ C$ above normal. While southern Norway had only about 60 % of normal precipitation, northern Norway as a whole had close to normal precipitation, but with local variations. Thermal stress on vegetation was exceptional not only in large parts of Fennoscandia but also in much of Europe, where the influence of the high-pressure system extended even over five months (April/May, July–September). These conditions gave rise to massive forest fires in different parts of Europe and thus an increase in ozone precursors. Boreal wildfires emit in addition to CO_2 also CO ($[CO]/[CO_2] \propto 6 - 13\ %$) and VOCs ($[VOCs]/[CO_2] \propto 0.5 - 1.5\ %$)

(Cofer et al., 1990). A total of 2079 forest fires of different sizes were registered in Norway in 2018, twice as many as in the preceding years 2016/17 (DSB, 2019), last accessed April 2020). In Sweden, about 500 fires had been reported (five times more than in a usual summer), and an estimated total of 25000 hectare burned down in central Sweden (Gävleborgs, Jämtlands, and Dalarnas län) (Björklund et al., 2019). Coincident peak [O₃] is found in ozone monitoring data from Svanhovd (Fig. 2 but also over whole northern Fennoscandia in July. During the 2003 drought period, elevated ozone in Europe was promoted by a combination of various factors such as wildfires, reduced cloud cover (increased solar radiation), reduced dry deposition and turbulent mixing due to the stagnant weather conditions, and increased BVOC emissions (Solberg et al., 2008). It is likely that these factors also contributed to enhanced [O₃] in 2018.

135

The described methods for risk assessment rely on accurate representation of plant physiological response to key environmental variables and are most often parameterized using data for less extreme climates, i.e., temperate or continental climates; and to a lesser extent, Boreal and Mediterranean climates. Parameterization of these models for more extreme bio-geographical regions such as subarctic climates has not been performed and relies on assuming that less extreme Boreal parameterization will be applicable. It is important to understand the implications of using these more generic parameterizations for more extreme climate regions. We explore how risk estimates might be over or underestimated using generic vs bespoke subarctic parameterization. We also explore the role of [O₃] variability and changing climate variables to understand how this risk might alter in the future with the advent of climate change. To this end, conditions at Svanhovd for the growing seasons 2018/19 shall serve as a reference for present and probable future conditions in northern Fennoscandia. This allows an understanding of how the threat from ozone may change in the future and which are the key aspects of plant physiology that might determine the potential risk. Hence, we determine which parameters require special attention to define accurately for pollution impact assessment and more generally for describing gas exchange response to a changing climate that will influence biochemical cycling. This might also be one key to solve long-standing issues of earth system models (ESM) which often lack PFTs specifically representing subarctic conditions in their land surface models (Poulter et al., 2015; Lawrence et al., 2019).

140
145
150

The observation site at NIBIO Environment Centre Svanhovd and all related data are presented in Section 2. In Section 3, we derive multi-annual means for ground-level ozone concentration and key environmental variables (temperature, precipitation, and global irradiance) based on in situ observations and evaluate the deviation of 2018/19 from the norm. We use the DO₃SE model to estimate the ozone uptake by natural and semi-natural vegetation to investigate the main environmental drivers for projected ozone damage risk in 2018 (Section 4). To this end, we derive bespoke parameterizations for subarctic species to assess systematic uncertainties arising from the use of generic parameterizations established from less climatically extreme conditions. In Section 5, we will summarize our results and discuss how this research can support improvements in future assessments of pollution risk and more generally biogeochemical cycling.

2 Data acquisition

160 In our assessment of primary drivers of ozone damage risk on vegetation in the subarctic, we focus on conditions during the
161 2018/19 growing season at the NIBIO operated Environment Centre Svanhovd. We also set these into a climatological and
162 regional context. To this end, we collected atmospheric and ozone monitoring data taken at Svanhovd and additional ozone
163 monitoring data from observation sites in northern Finland and Sweden for cross-evaluation. Varying update frequencies and
164 length of available data sets made it necessary to fetch the data from various sources (further details below). Svanhovd synonym-
165 ously refers to the atmospheric monitoring site Svanvik/Pasvik throughout the paper.

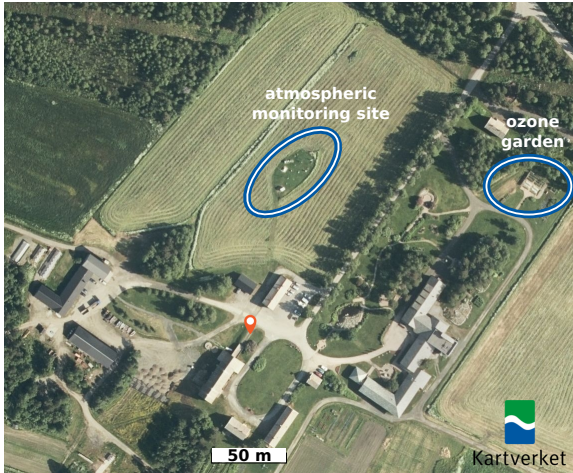
170 The foundation of the NIBIO Environment Centre Svanhovd dates back to the 1930s (NIBIO, b). The NIBIO centre Svan-
171 hovd is located south of the settlement of Svanvik, where the Pasvik river, which is the border to Russia, lies only a few hundred
172 meters to the east. It focuses on the research of the special environment of the region, but also comprises long-term observations
173 of various agrometeorological variables, i.e. 2 m temperature, precipitation, global irradiance, and soil temperature at different
174 depths.

175 To relate local ozone concentration ($[O_3]$) with visible damage on ozone sensitive plants, both an ozone bio-monitor (referred
176 to as ozone garden) and a conventional ozone monitor using the existing atmospheric monitoring infrastructure had been
177 installed during the 2018/19 growing season at the NIBIO centre. The locations of the atmospheric monitoring site and the
178 ozone garden are marked in the aerial photography shown in Fig. 1a). This ozone garden was likely the northern-most to date
TODO: Reference?. An ozone garden consists of selected plant species that are sensitive to ozone and are likely to display
179 visible injuries. Cultivated species were, e.g. clover, tobacco, and potatoes. As shown in Fig. 1b), the plants had to be protected
180 from herbivores with a wire-mesh fence. In 2018, we qualitatively observed visible ozone damage on semi-natural vegetation
(clover) and crops (tobacco). In contrast, no such visible damage was found on the clovers in 2019, although it was observed on
the sensitive tobacco cultivar. This indicates that the vegetation may have been more affected by ozone in 2018 than in 2019.

185 All measured atmospheric variables including ozone for the 2018/19 growing season were obtained through luftkvalitet.no
operated by NILU (a). The ozone monitoring data have been also added to the EBAS database operated by NILU (b) and
are thus openly accessible. All long-term ozone observation data described in Section 2.2 are also obtained from EBAS. The
long-term data sets of agrometeorological variables including temperature and precipitation are available from September 1992
to the present day (LandbruksMeteorologiske Tjeneste NIBIO, a, note the station name here is Pasvik).

2.1 2018/19 growing season

190 All relevant data for the growing season 2018/19 are shown as time series in Fig. 2. Ozone concentrations measured at 2 m
height above ground are averaged hourly. The hatched areas mark times when no ozone data were recorded. Note, while the
downtime during winter was planned, missing data in two weeks of July 2018 (July 9–23) were due to problems in data
acquisition.



(a)



(b)

Figure 1. NIBIO Environment Centre Svanhovd close by the settlement of Svanvik, Norway. (a) Atmospheric monitoring site and ozone garden have been marked. Aerial photography ©Norges Kartverk; (b) Clover in the Svanhovd ozone garden. The plants had to be secured against herbivores with a wire-mesh fence. The plants shown are approximately 6–12 cm high.

As can be seen in Fig. 2a), $[O_3]$ peaks in spring (April/May) and reaches its minimum in late summer (July/August). The spring peak has not been captured completely in 2019, since data acquisition only started in late April. In summer 2018 (June–August), high ozone concentrations ($[O_3] > 40$ ppb) were recorded 50 times. The highest summer ozone concentration ($[O_3] = 50.2$ ppb) was measured on July 25. This coincides with the period of the most extensive forest fires in central Sweden 195 which occurred from July 12–29 (Björklund et al., 2019). However, due to the above-mentioned data acquisition problems, we missed most of the corresponding ozone data for this event and most likely also the peak $[O_3]$. In contrast, $[O_3]$ only rose 18 times above the threshold of 40 ppb during the summer of 2019. For further analysis (Section 3) and modeling study with

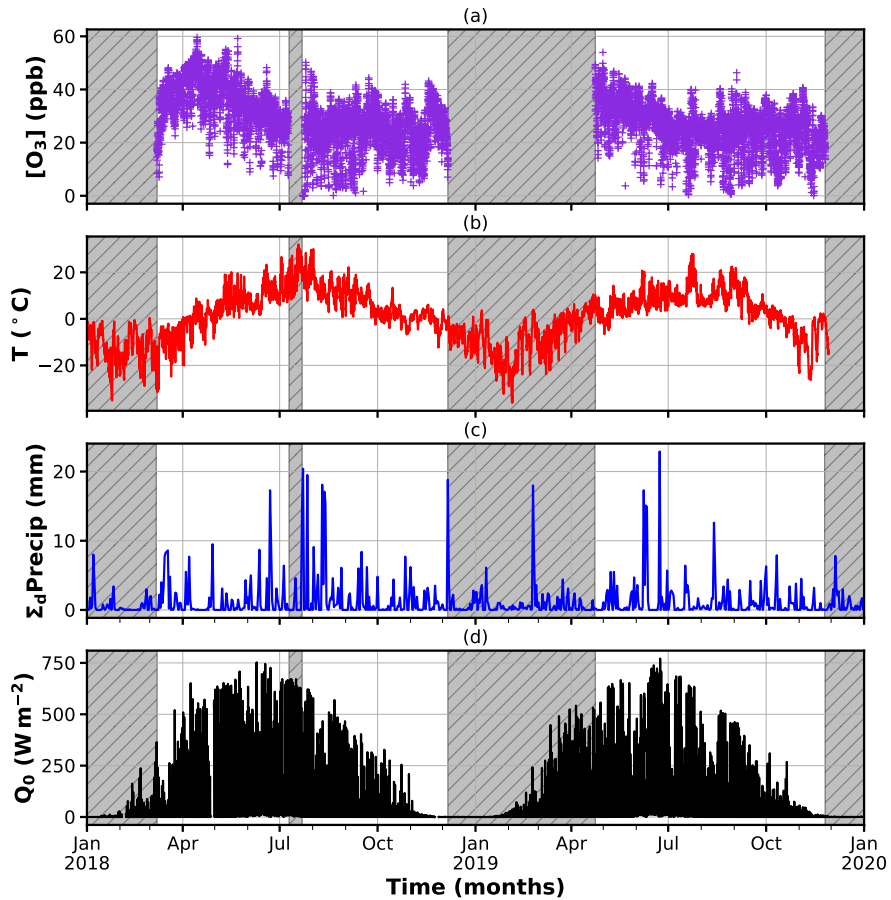


Figure 2. Observational data from atmospheric monitoring at Svanhovd in 2018/19. The hatched areas indicate periods without ozone monitoring data. (a) Hourly averaged $[O_3]$; (b) hourly averaged temperature; (c) daily accumulated precipitation; (d) hourly averaged global irradiance.

the DO_3SE model (Section 4), we reconstructed the missing data. The used gap-filling method will be described in detail in a companion paper.

200 Hourly averaged 2m temperatures above 20°C occurred more regularly in July 2018 than in 2019 (Fig. 2b). In 2018, spring temperature regularly rose above freezing only in May, while in 2019 this occurred already early in March/April. More rain events with accumulated daily precipitation ($\sum_d \text{Precip}$) above 10mm occurred in the summer of 2018 compared to 2019 (Fig. 2c). Qualitatively, global irradiance (Q_0) displayed in Fig. 2d) was higher in May and July 2018 compared to 2019, while June 2019 showed higher irradiance than 2018. A high global irradiance in most cases is the result of a low cloud fraction. In 205 both years, the maximum recorded Q_0 was 750 W m^{-2} and reached in June.

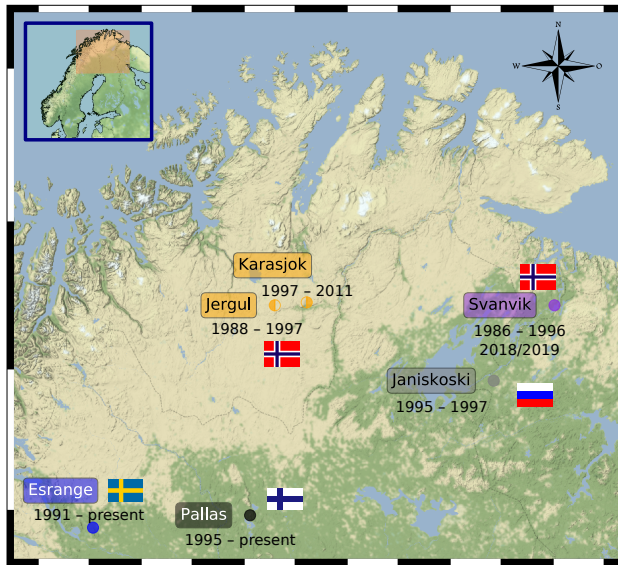


Figure 3. Cap of the North. Locations of past and present (end of 2018) ozone observation sites in northern Fennoscandia were used in this study. For more details see Table 1. The same color coding for each station as displayed herein will be used in all the following figures.

2.2 Ozone data

From 1986–1996, ozone monitoring has been operated continuously by NILU at Svanhovd, but no ozone measurements have been conducted before the 2018/19 growing season. To determine the significance of the $[O_3]$ in 2018/19 in relation to regional trends, we derive a ground-level $[O_3]$ climatology for Svanvik and northern Fennoscandia in general (Section 3).

210 A comprehensive overview over all past and present ozone observation sites in northern Fennoscandia is given in Table 1 and Fig. 3, respectively. All stations with available long-term observations are located at higher altitude than Svanhovd. In the absence of local precursors, the stratification of the atmosphere usually leads to a higher abundances in ozone at higher altitude (e.g., Klingberg et al., 2009). The periphery vegetation at all sites is similar and consists mainly of pine forests, birch, perennial grassland, and heath. However, on closer inspection the vegetation differs substantially. Ozone measurements at 215 Pallas are taken on top of mount Sammaltunturi, 100 m above treeline (pine forest), and the surrounding vegetation mainly consists of low vascular plants, mosses, and lichen (Hatakka et al., 2003). At Svanhovd, the ozone measurements are taken amidst a meadow surrounded by agriculturally managed herbaceous plants and grass adhering to the WMO (2018) standards (Fig.1). In conjunction with the location at lower altitude, this results in generally lower $[O_3]$ at Svanhovd compared to Pallas.

220 Data from before the 1990s are available solely from Svanvik and Jergul. These data, however, do not follow the high-quality standard procedures implemented nowadays and have to be treated with care (Solberg, 2003). Especially, ozone monitors did not undergo regular re-calibration. This probably leads to drifts in the observed data and may impose a false trend. In 1997, the ozone monitoring at Jergul was relocated downstream of the river Karasjokka to a site close by Karasjok. Although the same equipment has been used, this might have introduced a baseline shift in the combined data series, denoted as Jergul/Karasjok,

Table 1. Past and present ozone observation sites in northern Fennoscandia. Data available on EBAS.

Name	Country	ID	Location			Operational
			lat	lon	alt	
			(°N)	(°E)	(m)	
Esrangle	SWE	SE0013R	67.83	21.07	475	1991 – 2018 ¹
Janiskoski	RUS	RU0001R	68.93	28.85	118	1995 – 1997
Jergul	NOR	NO0030R	69.45	24.60	255	1997 – 2011
Karasjok	NOR	NO0055R	69.467	25.217	333	1988 – 1997
Pallas	FIN	FI0096G	67.97	24.12	565	1995 – present ²
Svanvik	NOR	NO0047R	69.45	30.03	30	1986 – 1996 ³

¹ Data available on EBAS until the end of 2018.

² Data available on EBAS until the end of 2019.

³ Exclusive ozone monitoring in growing seasons 2018/19 for the present study operated by NILU.

which would be particularly problematic if these were the sole data for comparison. Only a few data have been taken upstream
225 the Pasvik river at Janiskovski, hence these will not be taken into further consideration, but are listed for completeness. There
is an overlap of about 4 years between data taken at Esrange, Jergul/Karasjok, and Svanvik (Supplement Fig. S1).

3 Statistical analysis

In this section, we assess the climate conditions. To this end, we compute multi-annual mean (referred to as climatology in the
following) of environmental key variables (temperature, precipitation, global irradiance) and ground-level [O₃] at Svanhovd.
230 For the growing seasons 2018/19, we evaluate the statistical significance of divergences from the norm in these variables
(referred to as anomalies). We perform a bias correction accounting for the increase in tropospheric background [O₃] and
cross-calibrate the derived climatology for Svanvik with long-term observations of [O₃] at Esrange and Pallas.

3.1 Derived climatologies

3.1.1 Temperature, precipitation, and global irradiance

The location of Svanvik at 69.45°N suggests a subarctic climate. The derived climate diagram based on climatological data
235 (1992–2012) (Fig. 4) supports this very well. Monthly averaged 2 m temperatures (red line) are displayed with a standard error
of the mean (SE) as error band. We chose SE in this case due to the large interannual variability in temperature reflected in
the standard deviation. Averaged monthly accumulated precipitation (blue bars) is shown with standard deviation as error bars.
Months with average temperatures below freezing are denoted with a star. As can be seen, temperatures stay below freezing
240 for 5 consecutive months, while only 2 months breach 10 °C regularly (July, August), satisfying the conditions for Köppen's
climate classification of a regular subarctic climate (Dfc) (e.g. Beck et al., 2018). The highest monthly average temperature is

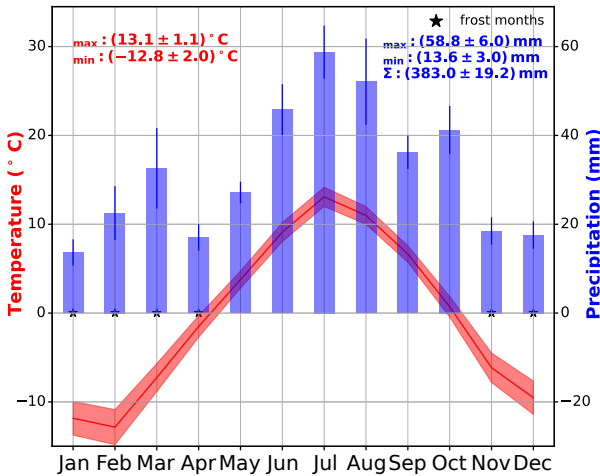


Figure 4. Climate diagram following Walter and Lieth. The diagram is based on climatological data for Svanvik/Pasvik (1992–2012). Monthly averaged temperatures (red line) are displayed with standard error of the mean as error band. Averaged monthly accumulated precipitation (blue bars) is shown with a standard deviation of mean as error bars. Months with average temperatures below freezing are denoted with a star.

(13.1 ± 1.1) $^{\circ}\text{C}$ in July and the lowest (-12.8 ± 2.0) $^{\circ}\text{C}$ in February. In the period 1992–2012, the coldest measured temperature was -45.2 $^{\circ}\text{C}$ observed January 27, 1999, while the highest temperature (29.4 $^{\circ}\text{C}$) occurred July 16 the same year.

The average accumulated monthly precipitation ($\sum_d \text{Precip}$) indicates that winter and spring (November–April, except for 245 March) are relatively dry ($\sum_d \text{Precip} < 20$ mm). The driest month is January with $\sum_d \text{Precip} = (16.7 \pm 3.0)$ mm. The most precipitation occurs in the summer months, with a $\sum_d \text{Precip} = (58.5 \pm 9.2)$ mm in August. The average annual accumulated precipitation ($\sum_m \text{Precip}$) given with standard error of mean is (383 ± 86) mm. Precipitation shows a large interannual variability.

The derived climatology for global irradiance (Q_0) at Svanvik (Appendix Fig. A1a)) approaches zero in December/January 250 (polar night) and reaches its maximum in June/July (midnight sun conditions). The highest observed averaged daily maximum ($\langle Q_0^{\max} \rangle$) amounts to 800 W m^{-2} , while the maximum of the averaged daily mean ($\langle Q_0^{\text{mean}} \rangle$) is 450 W m^{-2} (regularly reached in May–July). The maximum of the averaged daily minimum ($\langle Q_0^{\min} \rangle$) lies at about 200 W m^{-2} .

3.1.2 Ozone

In the following, we derive an ozone climatology ($\langle [\text{O}_3] \rangle$) for Svanvik and for northern Fennoscandia. To this end, we first 255 calculate a pairwise correlation between the different stations. The correlation of $[\text{O}_3]$ between Esrange, Pallas, and Jergul/Karasjok is fairly high ($r^2 \approx 0.8$, Appendix Fig. A2). Therefore, we select these data to compute the generalized ozone climatology for northern Fennoscandia. The correlation between Svanvik with any of the active monitoring sites in 2018

(Esrang and Pallas) is rather low, 0.4 and 0.6, respectively. Thus, conditions at Svanvik cannot directly be represented by measurements taken at either Esrange or Pallas.

260 In Figure 5, two dimensional density distributions of $[O_3]$ for the combined data (Esrang, Jergul/Karasjok, Pallas) (Fig. 5a) and Svanvik (Fig. 5b) are shown. Darker colors indicate higher probability to observe these values. On top of the density distributions, a 10 days average of daily mean ($\langle [O_3] \rangle_{10d}$) is displayed together with 1σ uncertainties and SE, respectively. Splines have been fitted through the data for easier inter-comparison.

265 The generalized northern Fennoscandic ozone climatology peaks at 48 ppb in late April (day of the year (doy) 100–120) and declines throughout the growing season until a minimum is reached in the beginning of September (240–250 doy) and amounts to 24–30 ppb. The turning points lie approximately in June and November. The build-up of the ozone spring peak takes about 7.5 months from minimum to maximum. The most pronounced increase in $\langle [O_3] \rangle$ coincides with rising temperatures and global irradiance. The depletion of ozone from maximum to minimum takes only 4.5 months.

270 The $[O_3]$ density distribution and the $\langle [O_3] \rangle_{10d}$ for Svanvik display a similar pattern as the generalized northern Fennoscandia climatology (Fig. 5b). The spring peak occurs slightly earlier (100 doy) and amounts to 40 ppb while the annual average $\langle [O_3] \rangle$ is 6.6 ppb lower than the Fennoscandic climatology. This is in line with a general decrease in tropospheric ozone with decreasing altitude. The earlier decline in $\langle [O_3] \rangle$ may point to an influence of coniferous vegetation on the removal of ozone since CO₂ uptake by coniferous trees has been observed as early as doy 100 (Kolari et al., 2007; Wallin et al., 2013). The estimated average begin of growing season for deciduous trees ($\langle G_{start} \rangle_{decid}$) is (150 ± 14) doy at Svanvik (see Section 4.1
275 for details). In July–September, ozone is occasionally almost completely depleted during nighttime. This hints to ozone uptake by vegetation even at low light intensities during midnight sun conditions in combination with stable planetary boundary layer conditions preventing mixing of ozone rich air. The derived $\langle [O_3] \rangle$ is likely biased towards lower $[O_3]$ due to an increase in northern hemispheric tropospheric background $[O_3]$ since the 1990s. To account for this, we derive a bias correction factor by cross-calibrating with the time series taken at Esrange and Pallas (Section 3.2).

280 3.2 2018/19 anomalies

In the following, we look at the 2018/19 anomalies and discuss the differences between the two years. We also conduct a bias correction for the Svanvik $\langle [O_3] \rangle$. As weather extremes like in 2018 are likely to become more frequent with climate change, this will help to assess possible future changes in the vulnerability of subarctic vegetation to ozone.

3.2.1 Temperature, precipitation, and global irradiance

285 In Fig. 6a), temperature anomalies for Svanvik are shown as a percentage of days warmer or colder than $\pm 1\sigma$ from the climatological mean for each month. Negative deviations from climatology are displayed as a negative percentage. The annual positive/negative deviations are indicated in the respective corners (right upper/right lower). The hatched area between the dashed lines indicates the expected percentage of values falling above/below $\pm 1\sigma$ if a normal distribution is assumed (15.9%). We find, that the summer of 2018 was significantly warmer than average. Especially in May and July more than 40% of the
290 days were significantly warmer. Significantly warmer days continued to occur in all months (August–November) except for

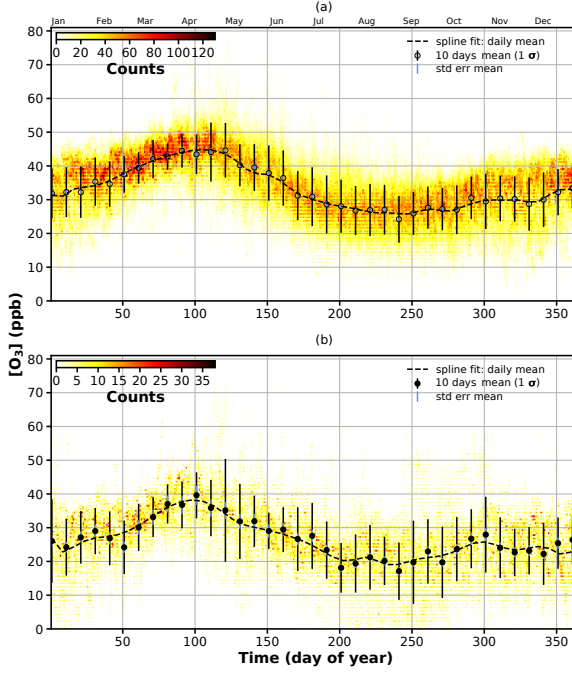


Figure 5. Ozone climatologies. Fennoscandia combines all available data from Jergul/Karasjok, Esrange, and Pallas. The density distributions are shown together with a multi-annual mean of daily $[O_3]$ (climatology). Splines have been fitted through daily mean $[O_3]$. The climatology of daily mean ozone is shown together with 1σ standard deviation and standard error of the mean. Since $[O_3]$ are strongly correlated for sites at Jergul/Karasjok (NOR), Esrange (SWE), and Pallas (FIN) (see Fig. A2), data of these have been averaged together to derive a climatology for northern Fennoscandia. (a) Northern Fennoscandia; (b) Svanvik.

October. March 2018 had many unusually cold days. The summer of 2019 was fairly average, however, significantly colder days occurred in July, while August had both significantly colder and warmer days. April 2019 had significantly warmer than average days.

Similarly, the precipitation anomalies for Svanvik are displayed in Fig. 6b). Due to the large interannual variability in 295 observed precipitation, only a few days deviated significantly from the climatology on the 1σ level. Therefore, we lowered the σ level constraint to $\pm\frac{1}{2}\sigma$. The percentage of days wetter/drier than $\pm\frac{1}{2}\sigma$ are shown for each month. Positive deviation refers to days wetter than average and negative deviation to drier than average. The hatched area between the dashed lines indicates the expected percentage of values falling above/below $\pm\frac{1}{2}\sigma$ if a normal distribution is assumed (30.8%). Unlike the 300 temperature anomalies, the picture is not as clear. While March 2018 had a significant number of days wetter than unusual, summer and fall (May/July, September/October) had a significant number of days drier than average. 2019 was rather average throughout the year, but with a significant number of days drier than normal in September/October and wetter in December.

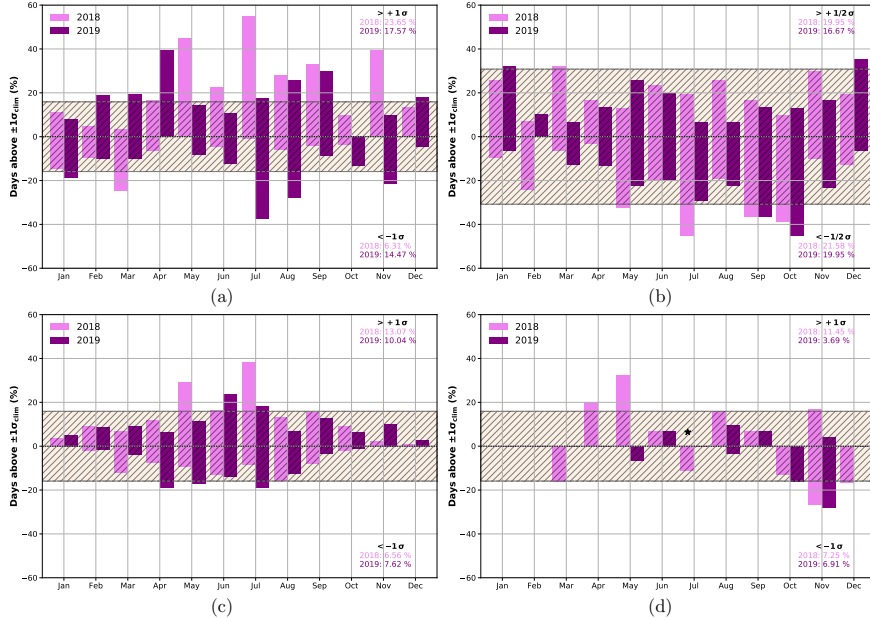


Figure 6. 2018/19 anomalies of key environmental variables at Svanhovd displayed as percentages of days significantly deviating from climatological mean through standard deviation for each month. Negative deviations from the climatology are shown as a negative percentage. The annual positive/negative deviations are indicated in the respective corners (right upper/right lower). The hatched area between the dashed lines indicates statistical significance under the assumption of a normal distribution (15.9 %, 30.8 % for Precip.). (a) Temperature; (b) precipitation; (c) global irradiance; (d) ozone.

The global irradiance anomalies for Svanvik are presented in Fig. 6c). The percentage of days above or below $\pm 1\sigma$ from the climatological mean is displayed for each month. The hatched area between the dashed lines indicates the expected percentage of values falling above/below $\pm 1\sigma$ if a normal distribution is assumed. In summer 2018 (May/July), global irradiance showed
 305 a significant number of days with higher than average irradiance, while 2019 was generally an average year with a significant number of days darker in spring (April/May).

In summary, 2018 had a significant number of days that were warmer, drier, and brighter than the climatological average, while 2019 was a rather average year.

3.2.2 Ozone

310 To assess the significance of 2018/19 anomalies, we estimate the bias due to the change in the tropospheric background $[O_3]$ since the 1990s and account for the missing data in June 2018. To reconstruct these missing data, we performed a Reynolds decomposition (Eq. (B9)) and cross-calibrate with ozone observations at Esrange and Pallas (companion paper). In the following, we will describe the bias-correction and discuss the significance of $[O_3]$ enhancements in 2018.

In 2018, the probability density functions (PDFs) of ozone concentration anomalies ($\Delta[\text{O}_3]$) for Esrange and Pallas deviate
315 clearly, but not significantly from the climatological mean (Supplement Fig. S2). On average, $[\text{O}_3]$ had been elevated by
(1.9 ± 5.7) ppb and (1.9 ± 5.4) ppb, respectively. Both distributions are slightly skewed towards positive deviations with $\frac{1}{4}$ of
days (3. quantile, q3) falling above 5.8 ppb and 5.6 ppb, respectively.

We find a similar skew towards higher $[\text{O}_3]$ for Svanvik in 2018, while 2019 follows a normal distribution rather well
(Supplement Fig. S3). In conjunction with the meteorological conditions, we therefore assume that 2019 had been a normal
320 year and the annual average anomaly in 2019 ($\langle \Delta[\text{O}_3] \rangle = (1.2 \pm 5.0)$ ppb) can be used for the bias correction. We also consult
the trends in ozone observations at Esrange and Pallas to strengthen this assumption and compute the average difference
between recent years and the mid 1990s ($\Delta_{\text{present} - \text{past}} \langle [\text{O}_3] \rangle$). Herein, present is defined as the average over 2010–2018
and past as the time between the respective beginning of data taking until 1997. We do not find a clear trend. For Esrange
325 $\Delta_{\text{present} - \text{past}} \langle [\text{O}_3] \rangle$ amounts to (1.5 ± 3.1) ppb and for Pallas to (-2.5 ± 3.7) ppb (Solberg, 2003; Ruoho-Airola et al., 2015,
for comparison). Only the observed trend at Esrange is compatible with our assumed bias correction for the Svanvik ozone
climatology.

In accordance to the above findings, we adjust the derived ozone climatology for Svanvik by adding a constant bias correction
factor $\Delta[\text{O}_3]_{\text{bias-corr}} = 1.2$ ppb and assess the monthly significance of the ozone concentration anomalies in 2018/19. The
resulting percentage of days above/below $\pm 1\sigma$ from the bias-corrected climatological mean is displayed for each month in
330 Fig. 6d). Negative deviations from climatology are shown as a negative percentage. Note that missing bars for certain months
are both due to data availability and anomalies not meeting the 1σ criteria. The star indicates results after the reconstruction
of missing data in July. In April/May 2018, ozone was significantly enhanced, while no significant enhancement is found in
2019. In both years, ozone concentrations were significantly lower than average in November. These results indicate that the
extensive forest fires in Sweden did not contribute to a significant enhancement in $[\text{O}_3]$ at Svanhovd in 2018, but the stagnant
335 meteorological conditions in April/May in combination with a late start of the growing season. However, there are indications
that the sites further south at Esrange and Pallas experienced more days of elevated ozone in 2018 than Svanvik.

4 DO₃SE modeling

In the following, we investigate the difference between 2018 and 2019 concerning stomatal ozone uptake and assess which of
the environmental factors might be most influential in determining O₃ damage risk. We model ozone uptake of natural and
340 semi-natural vegetation using the DO₃SE model and develop bespoke subarctic parameterizations for common plant species.
First, we give an account of the methodology for deriving bespoke parameters, after which we present and discuss the modeling
results. The DO₃SE model and conducted gap-filling methods are described in Appendix B.

4.1 Model parameters

We deduced the dominant species on-site at the NIBIO Environment Centre Svanhovd and from Fig. 1 and found perennial
345 grassland, birch (generalized as deciduous trees), and Scots pine (generalized as coniferous trees). Default parameters for these

species or PFTs are derived from Simpson et al. (2007); Mills et al. (2011, 2017) and will be referred to as *mapping manual* (MM) parameterizations in the following. We base our parameterization of coniferous trees on the MM's Boreal Norway spruce and deciduous trees on the MM's silver birch. For a comprehensive list of model parameters, consult Supplement Table S1.

Initial test simulations with the MM PFTs revealed an unrealistically low stomatal conductance at leaf-level ($G_{\text{sto}}^{\text{leaf}}$) in 2019
350 particularly for perennial grassland (Appendix Fig. B1). Substantial stomatal conductance occurred only during an extended warm period in late July. In ecological terms, this means that there was almost no growth of grass in the summer of 2019 – a prediction which is easily falsified by reality. We identified f_T as abnormally low, being the limiting factor of stomatal conductance in perennial grassland. Therefore, we saw the necessity to propose bespoke parameterizations describing an acclimation of the PFTs to the climatic conditions in the target region. Note, however, that these parameterizations are hypothetical and
355 have yet to be verified by experiments.

We hypothesize that perennial vegetation will likely prioritize growth and hence their carbon acquisition during the short subarctic growing season. Because the mapping manual version of the DO₃SE model currently does not simulate net photosynthesis (A_n), we assume a first order proportionality between A_n and g_{sto} (Medlyn et al., 2011) and effectively tune the temperature and light response functions (f_T and f_{light}) for higher $\langle g_{\text{sto}} \rangle / g_{\max}$ (see Appendix B for details) to acclimate the
360 growth potential to the local climate. We further assume that f_{VPD} and f_{SWP} suit our biomes. The procedure is graphically illustrated in Fig. 7 for grassland. We aim to increase the enclosed area between the probability density function (PDF) and the respective response function. We show two climatological reference periods 1990s and 2000s to indicate that the vegetation is subject to ongoing climate change and hence continuous acclimation. The resulting response functions for coniferous and deciduous trees are displayed in Appendix Figs. B3–B4, respectively.

365 We define two different hypothetical temperature acclimations: *subarctic* and *cold*. For either, we assume that the hypothetical species are more tolerant to cold conditions and shift f_T towards colder temperatures accordingly. We construct *cold* as representative for a species that is more tolerant to cold temperatures, but slightly less efficient at warm temperatures compared to MM. In the same way, *subarctic* refers to a hypothetical species which is very tolerant to cold but is sensitive to high temperatures, and most efficient at cool temperatures (T_{opt} close to the climatological mean temperature of 1992–2000). The
370 most extreme of the two acclimation types is *subarctic*. For perennial grassland the resulting response functions are depicted together with a five month growing season temperature PDF of the two periods 1992–2000 and 2011–2019 in Fig. 7a).

Norway spruce was experimentally found to be active already at rather low air temperatures and can reach 60 % photosynthetic activity as early as doy 100 (Kolari et al., 2007; Wallin et al., 2013). Based on the time series of CO₂ uptake and temperature at observation sites in southern (→ *cold*) and northern (→ *subarctic*) Finland (Kolari et al., 2007), we estimate
375 the optimal temperature interval $10^\circ\text{C} \leq T_{\text{opt}} \leq 15^\circ\text{C}$. We assume similar temperature acclimations for deciduous trees. All bespoke temperature parameters are listed in Table 2.

With respect to light conditions, we assume that the light threshold for a 50 % opening of plants' stomata may differ in subarctic species compared to species in less extreme climates. Analytically, we derive the inverse function $f_{\text{light},k}^{-1}$ of Eq. (B4)

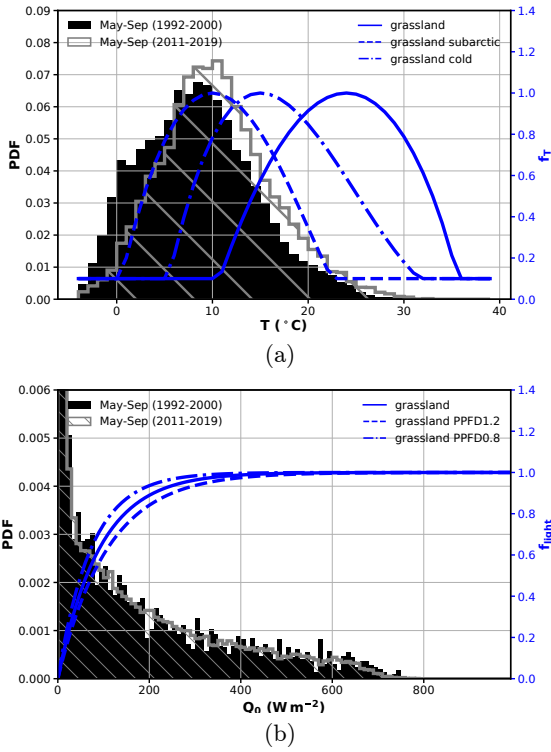


Figure 7. Construction of bespoke response functions for grassland. (a) f_T and (b) f_{light} are shown together with underlying T_{air} and Q_0 climatologies (probability density function - PDF), respectively. Original mapping manual parameterization is shown in comparison as solid line. Note that Q_0 has been truncated to 0.006. PPFD0.8 and PPFD1.2 refer to α values increasing/decreasing PPFD at $f_{\text{light}} = 0.5$ by $\pm 20\%$, respectively.

for each PFT or species k

$$380 \quad \gamma_k(f_{\text{light}}) := f_{\text{light},k}^{-1} = -\frac{\ln(1-f_{\text{light}})}{\alpha_k}. \quad (3)$$

First, we solve Eq. (3) for the MM default value α_{MM}^k for each PFT or species k at 0.5

$$\gamma^k(0.5) = -\frac{\ln(0.5)}{\alpha_{\text{MM}}^k}, \quad (4)$$

and define a variation $\gamma' = \gamma \cdot \eta$ with $\eta \in \{0.8, 1.2\}$. We invert Eq. (3) for α and find $\alpha'(\gamma')$. The resulting functions for perennial grassland are shown in Fig. 7b) (for deciduous and coniferous trees refer Appendix Figs. B3b)–B4b)). All derived parameters are tabulated in Table 3.

As indicated above, a better acclimation to prevailing climate conditions will result in a higher average $\langle g_{\text{sto}} \rangle / g_{\text{max}}$. To quantify the resulting bespoke parameterizations, we propose the following metric. For a generic GS (May–August), we compute

Table 2. Bespoke temperature parameterizations. MM refers to mapping manual (Mills et al., 2011, 2017).

Species	type	T_{\min}	T_{opt}	T_{\max}
Deciduous tree	MM	5	20	100
	Cold	5	15	100
	Subarctic	0	10	100
Coniferous tree	MM	0	20	100
	Cold	0	15	100
	Subarctic	0	10	100
Perennial grassland	MM	10	24	36
	Cold	5	15	36
	Subarctic	0	10	24

Table 3. Bespoke light parameterizations. MM refers to mapping manual (Mills et al., 2011, 2017).

Species	type	α	$\gamma(0.5)$
Deciduous tree	MM	0.004	165.035
	PPFD0.8	0.005	132.028
	PPFD1.2	0.003	198.042
Coniferous tree	MM	0.006	115.525
	PPFD0.8	0.008	92.420
	PPFD1.2	0.005	138.629
Perennial grassland	MM	0.011	63.013
	PPFD0.8	0.014	50.411
	PPFD1.2	0.009	75.616

climatological average and standard deviation of $\langle g_{\text{sto}} \rangle / g_{\max}$ (Eq. (B1)) at noon (averaged over 11 am – 1 pm local time) and in the morning (averaged over 5 – 9 am local time). We presume that relative stomatal conductance around noon (highest light intensity) and in the early morning (lower intensities) are good proxies for CO₂ uptake efficiency. Our arbitrary optimization target is 60 %. Additional constraints are a small deviation between noon and morning and a low standard deviation indicating a higher robustness to interannual variability of growing conditions. For simplicity, we neglect the dependency on SWP in this metric. From the results shown in Fig. 8, we identify *subarctic*, PPFD0.8 as the best acclimation for all PFTs alike. As expected due to the small adjustments, coniferous trees display the lowest deviation between the different types of acclimation, while the divergence for perennial grassland is substantial as a response to the stronger proposed temperature acclimation.

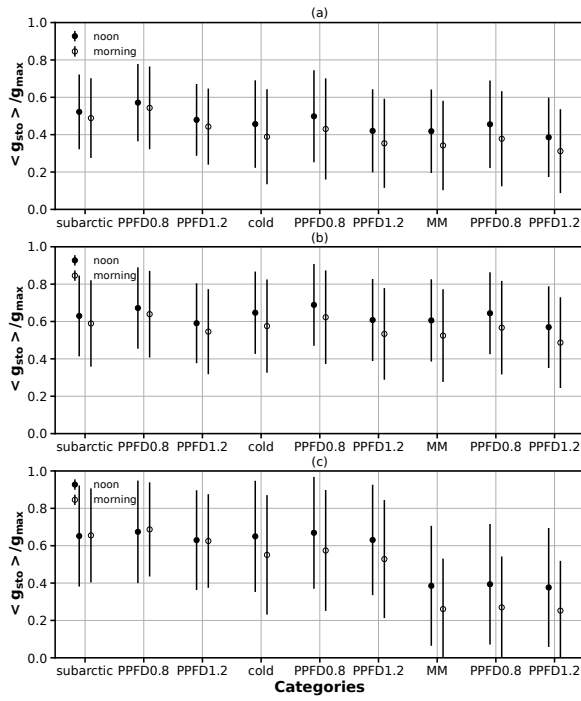


Figure 8. Proposed metric to test bespoke response functions. GS (May–August) climatological averages and standard deviation of g_{sto}^k (Eq. (B1)) relative to g_{max}^k at noon (averaged over 11 am – 1 pm local time) and in the morning (averaged over 5 – 9 am local time) are shown for (a) deciduous trees; (b) coniferous trees; (c) perennial grassland. Since f_{SWP} is connected to a plant hydraulic model within DO₃SE it is left out in this calculation.

Another important factor for ozone exposure metrics is the timing and length of the GS. Start (A_{start}) and end (A_{end}) of GS for each PFT are given in units of doy (Table 4) and estimated as follows. Coniferous trees show photosynthetic activity already at low temperatures (Wallin et al., 2013; Kolari et al., 2007). We use a MODIS (Aqua/Terra) retrieved net photosynthesis product (reference?) for a 1 × 1 km patch centered at Svanhovd to determine A_{start} and A_{end} . The net photosynthesis vs. time of year 400 data can be approximated by a second order polynomial function (Fig. B2). By calculating the roots of the fitted polynomial, we derive $A_{start} = 122$ doy for 2018 and doy 106 in 2019. A_{end} amounts to doy 261 and 274, respectively. This value will be used for all PFTs alike. The resulting growing season for coniferous trees in 2019 was one month longer than in 2018. For estimating A_{start} of deciduous trees, we use the 5 consecutive days above 5 °C agricultural rule of thumb on gridded temperature 405 data from SeNorge.no (Supplement Fig. S6). We find 129 and 130, respectively. For both years, these dates coincide with the first snow-free day at the closest inland meteorological weather station at Øvre Neiden (Sør-Varanger, NOR). For comparison, we would get $A_{start} = 100$ doy and $A_{end} = 307$ doy from the latitude model typically used for localizing DO₃SE. The latitude 410

Table 4. Bespoke start and end of growing season in units of doy. MM refers to mapping manual (Mills et al., 2011, 2017).

Species	Year	A_{start}	A_{end}
Deciduous tree	2018	129*	261†
	2019	130*	274†
Coniferous tree	2018	122†	261†
	2019	106†	274†
Perennial grassland	2018	159‡	261†
	2019	161‡	274†

† MODIS (Aqua/Terra) net photosynthesis product;

* 5 days – 5 °C-rule, T_{air} from seNorge.no;

‡ One month after snow melt; reference station Øvre Neiden
(Sør-Varanger, NOR)

model indicates a 2 month longer growing season. Due to a lack of quantitative field observation, we assume a latency period of 1 month after snow-melt for perennial grassland A "start".

As pointed out by Büker et al. (2012), a very important factor in deriving a proper POD_y is the soil texture or how much water the soil can hold. As Svanhovd is located in the bed of the Pasvik river, we assume a sandy loam texture at 60 cm depth. The estimate of leaf boundary layer resistance is a function of wind speed which will be influenced by the tree height and leaf dimensions. Leaves of downy birch in northern Fennoscandia are probably smaller than the 5 cm from the MM parameterization of silver birch leaves. A sample of downy birch leaves collected at Svanhovd had lengths of (3.0 ± 0.5) cm. In addition, Systad et al. (2004, p. 52) indicate an average tree height of 13.5 m in the area. Both factors will affect leaf boundary layer resistance, the smaller leaves would tend to reduce leaf boundary layer resistances whilst the shorter trees would reduce canopy roughness and increase canopy boundary layer resistances and hence the uptake of O_3 . In addition, one Scots pine forest at Svanhovd has been studied as a part of the ICP Forest mapping. Heights were measured in 2004, when the stand was 90 years old. Mean tree height was 10.1 m and maximum height was 16.2 m (Volkmar Timmerman, pers. comm.). Canopy height and leaf size are adjusted to local values in the models with bespoke growing season (GS bespoke) in the following.

420 4.2 POD_1 results and implications on ozone impact

We have modeled POD_y with a flux threshold $y = 1 \text{ nmol m}^{-2} \text{ s}^{-1}$ per projected leaf area (PLA) for the three natural/semi-natural vegetation types, deciduous trees, coniferous trees, and perennial grassland using the generic MM parameterization and our bespoke temperaure (*cold, subarctic*) and light (PPFD0.8, PPFD1.2) acclimation types, and localized GS. The results are shown in Fig. 9. For comparison, critical levels for a 4% (deciduous), 2% (coniferous) (refer to silver birch and Norway spruce in Mills et al., 2017), and 10% (perennial grassland, above ground) (Hayes et al., 2021) reduction in biomass are shown as horizontal dashed lines. Results for 2018 are color-coded in pink and 2019 in purple. Simulations with MM GS, canopy, and leaf parameters are indicated with squared markers, bespoke GS, canopy, and leaf parameters with circles. The annotation \pm

refers to the bespoke light response function (+ → PPFD1.2, – → PPFD0.8), while bespoke temperature response functions are indicated by categories on the x-axis. Closed/open symbols represent SWP sensitivity switched off/on in the model.

430 The results depicted in Fig. 9 allow for a comprehensive assessment of a large variety of systematic uncertainties in the exposure-based risk metric for ozone induced damage in subarctic vegetation. In summary, we identify the following main effects of the bespoke parameterizations of the DO₃SE model with respect to the MM default parameterization on ozone uptake:

- Increasing cold tolerance/heat intolerance ⇒ increased uptake in both probed years,
- 435 – usage of proper growing season ⇒ reduced uptake with respect to the increase reported above,
- an earlier assumed start of GS ⇒ increased uptake,
- drought conditions (SWP) ⇒ reduced uptake,
- lower/higher extent of stomatal opening at low light intensities ⇒ increased/reduced uptake,
- symmetric variation of the extent of stomatal opening at low light intensities ⇒ asymmetric response in POD,
- 440 – temperature acclimation ⇒ amplifying effect on light threshold and drought effects.

The magnitude of these effects varies between PFTs as well as years, but the predicted ozone uptake for the bespoke parameterization is always larger than for the MM default parameterizations and of the same order of magnitude as the variability between the years studied here. Although our temperature acclimations are hypothetical, they suggest considerable underestimations of ozone risk for subarctic species when relying on generic MM parameterizations. In particular, an earlier GS due to
445 climate change, that is overlapping with the ozone spring peak, has the potential to increase the risk of ozone damage for vegetation with an acclimation to cold climates. Drought effects (SWP) do only matter if a bespoke GS is not taken into account. We will look at the specific PFTs in more detail in the following.

For deciduous trees (Fig. 9a) all POD1 simulations exceed the CL by 5 – 25 mmol O₃ m⁻². Deciduous trees display the largest variance of ozone uptake among all PFTs (10 – 31 mmol O₃ m⁻²). In particular, the sensitivity to the light threshold is
450 especially pronounced, e.g. $\Delta\text{POD}_1 = {}^{+2.5}_{-3.6}$ mmol O₃ m⁻² in case of the subarctic type without bespoke GS in 2019. Without bespoke GS, 2018 displays a higher ozone damage risk than 2019. However, taking the later start and overall shorter GS in 2018 into account (bespoke GS), this is reversed for the *subarctic* acclimation type. This can be partly explained by very high light response factors ($f_{\text{light}} > 0.8$) in the beginning of the GS in these simulations. Whether this is a bug or a feature of the DO₃SE model is not clear. SWP-induced reduction in ozone uptake is only effective in 2018 and without bespoke GS. The
455 temperature-acclimation dependent bias in ozone uptake deduced for bespoke GS ranges between (1.4 – 3.6) mmol O₃ m⁻² in 2018 and (2.7 – 7.7) mmol O₃ m⁻² in 2019. The maximum systematic deviations deduced from the –20% (superscript) and +20% (subscript) variation of the extent of stomatal opening at low light intensities amount to ${}^{+1.6}_{-2.3}$ mmol O₃ m⁻² and ${}^{+1.9}_{-2.7}$ mmol O₃ m⁻², respectively.

For coniferous trees (Fig. 9b), most simulations slightly exceed the CL (0 – 10 mmol O₃ m⁻²). Coniferous trees' parameterization was already well acclimated to prevailing temperatures from the beginning and therefore the least biased of the
460

generic MM parameterizations. Coniferous trees display a medium sensitivity to the variation in the light threshold, e.g. $\Delta\text{POD}_1 = {}^{+1.7}_{-1.3} \text{ mmol O}_3 \text{ m}^{-2}$ in case of subarctic type without bespoke GS in 2018. Taking the bespoke GS and canopy height into account, we find a higher ozone uptake in 2019 than in 2018 for all bespoke temperature response functions. The overall bias deduced from bespoke GS for subarctic and cold types with respect to MM range between $(0.5 - 1.0) \text{ mmol O}_3 \text{ m}^{-2}$ in 2018 and $(2.0 - 3.3) \text{ mmol O}_3 \text{ m}^{-2}$ in 2019. The maximum systematic deviations deduced from the -20% (superscript) and $+20\%$ (subscript) variation of the extent of stomatal opening at low light intensities amount to ${}^{+1.0}_{-0.8} \text{ mmol O}_3 \text{ m}^{-2}$ and ${}^{+1.3}_{-1.0} \text{ mmol O}_3 \text{ m}^{-2}$, respectively.

For perennial grassland (Fig. 9c), all simulations with bespoke GS stay below the CL. Perennial grassland shows the smallest ozone uptake, but a similarly large bias as deciduous trees. We also find a reversal for predicted ozone damage risk in POD_1 between 2018 and 2019 for the subarctic type. Perennial grassland shows the lowest sensitivity to the light threshold and SWP is only relevant without bespoke GS. The overall bias deduced from bespoke GS for subarctic and cold types with respect to MM ranges between $(2.2 - 3.4) \text{ mmol O}_3 \text{ m}^{-2}$ in 2018 and $(4.4 - 6.4) \text{ mmol O}_3 \text{ m}^{-2}$ in 2019. The lower maximum temperature tolerance in the subarctic compared to the cold temperature parameterization probably caused the lower POD_1 values calculated for 2018 in subarctic compared to cold climate, whereas this was not seen for 2019. The maximum systematic deviations deduced from the -20% (superscript) and $+20\%$ (subscript) variation of the extent of stomatal opening at low light intensities amount to ${}^{+0.3}_{-0.2} \text{ mmol O}_3 \text{ m}^{-2}$ and ${}^{+0.3}_{-0.3} \text{ mmol O}_3 \text{ m}^{-2}$, respectively.

We estimated the biomass reductions in accordance to the CLs in Mills et al. (2017); Hayes et al. (2021) for the most extreme temperature acclimation (*subarctic*) for each bespoke PFT. The estimates are listed in Table 5. The reported range in uncertainty corresponds to the maximum deviation defined by the $\pm 20\%$ variation of the extent of stomatal opening at low light intensities with SWP=on. For deciduous trees and perennial grassland, substantial reductions in total biomass in comparison with the default generic MM parameterizations are predicted for both years. Coniferous trees are the least affected and the magnitude of total biomass reduction is independent of the choice of the parameterization within given uncertainties. This may reflect the more comprehensive research on this species or PFT feeding into the generic MM parameterization. The systematic deviation for deciduous trees is one order of magnitude larger than for coniferous trees and perennial grassland.

From the difference between 2018 and 2019, we infer a substantial interannual variability. The interannual variability is estimated to be larger than our reported systematic deviations and can be of the same order of magnitude as the effect of the temperature acclimation. This means that the choice of temperature acclimation has the potential to either revoke or amplify the risk of ozone damage for vegetation. However, the risk of ozone damage in deciduous trees and perennial grassland in comparison with the generic MM parameterizations is increased, regardless.

490 5 Discussion and conclusions

We have studied the effect of model acclimations of some common vegetation types to a subarctic climate on phytotoxic ozone uptake. The comparison between 2018 and 2019 conditions allowed us to consider these acclimations and their influence on vegetation sensitivity to O_3 in light of future changes of key environmental variables as may occur under climate change (e.g.

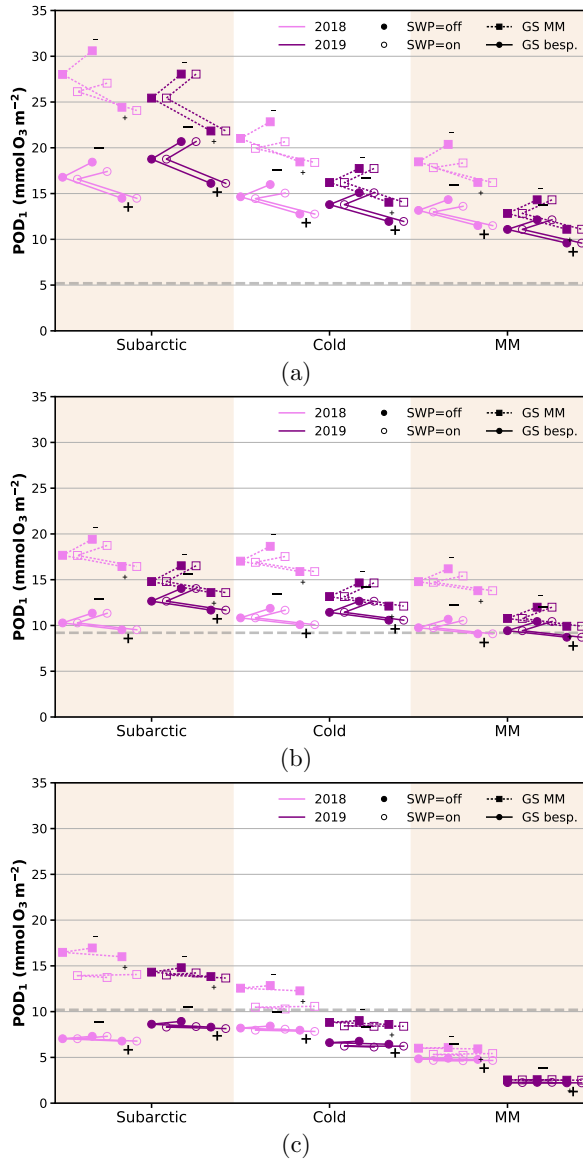


Figure 9. DO₃SE modeling POD₁ results for (a) deciduous trees, (b) coniferous trees, and (c) perennial grasslands at Svanhovd in 2018 (pink) and 2019 (purple). The results varied depending on parameterizations of temperature response functions (MM, Cold, and Subarctic, details in Table 2), growing season (GS MM (squares) or GS bespoke (circles), details in Table 4), light response functions (first, second and third point attached by a line are depicting the MM, PPFD0.8 and PPFD1.2, details in Table 3), and the effect of taking SWP into account (filled symbols without and open symbols with effects of drought kept in the model). Critical levels for ozone damage Mills et al. (2017); Hayes et al. (2021) are given as dashed horizontal lines. Note that the horizontal axis is only categorical.

Table 5. Estimated total biomass reduction in % for temperature acclimation *subarctic* with bespoke GS and SWP=off. The uncertainty ranges reported here correspond to maximum a divergence deducted from varying the extent of stomatal opening at low light intensities and SWP=on. For comparison, the corresponding biomass reduction for the generic default MM averaged over both years is shown. The reported standard deviation is computed from all sensitivity simulations ($\pm 20\%$ in extent of stomatal opening at low light, SWP on/off, and bespoke GS).

Year	PFT			
	Deciduous tree	Coniferous tree	Perennial grassland	
2018	$15.5^{+(1.9\dots 2.1)}_{-(0.8\dots 1.5)}$	$2.5^{+0.2}_{-0.2}$	$9.7^{+0.2}_{-0.2}$	$*12.4^{+0.2}_{-0.2}$
2019	$17.4^{+2.5}_{-1.8}$	$3.0^{+0.2}_{-0.3}$	$10.5^{+(0.1\dots 0.2)}_{-(0.0\dots 0.1)}$	$*13.7^{+(0.1\dots 0.3)}_{-(0.1\dots 0.3)}$
$\langle \text{MM} \rangle$	11.2 ± 1.1	2.31 ± 0.04	7.5 ± 0.9	$*9.6 \pm 1.4$

* above ground biomass

increase of frequency and extent of heatwaves). We found that conditions for ozone formation were more favorable in the 2018 growing season than in 2019, with 2018 being significantly warmer and less cloudy in spring and early summer. Accordingly, peak ozone concentrations occurred more frequently and at higher levels in 2018. This was particularly a result of the extended heatwave in spring and early summer and associated, extensive wildfires in Central Sweden (in particular in mid–end July).

We found that the length and timing of the growing season are crucial for risk assessment based on accumulated ozone flux metrics (POD_y). Based on a MODIS photosynthesis product, we estimated the growing season for coniferous trees in 2018 to be at least one month shorter than in 2019. The found start of growing season in 2018 (122doy) and 2019 (106doy) are within given ranges by empirical observations (Kolari et al., 2007; Karlsson et al., 2018). Based on gridded observational temperature and snow depth, we found a half a month shorter growing season for deciduous trees and perennial grassland in 2018 compared to 2019, respectively. The timing and emerging trend in the start of the growing season may differ substantially between local observation and common thermal or latitudinal estimations. Species-specific methods show a later start for European silver birch and an earlier for Norway spruce, compared to the thermal growing season (Karlsson et al., 2018). With respect to ongoing climate change, a clear positive trend in length ($5.2 \text{ d decade}^{-1}$) almost equally distributed between earlier start ($2.9 \text{ days decade}^{-1}$) and later end ($2.3 \text{ d decade}^{-1}$) could be deducted from the thermal growing season at Svanhovd.

Ozone peak concentrations were observed more frequently in 2018 than in 2019. In 2018, we found significantly enhanced $[\text{O}_3]$ particularly in April and May, but not during the active wildfires in July. This suggests that weather conditions and high ozone concentration at the beginning of the growing season are more important in risk assessment using flux-based metrics than episodes of peak concentrations over shorter periods. Because these peak $[\text{O}_3]$ may coincide with environmental conditions that limit ozone uptake and hence do not lead to damage. Consequently, acute cellular damage caused by very high fluxes over a short period is not accounted for properly in POD_y . As pointed out by Musselman et al. (2006), a higher temporal resolution, e.g. susceptibility to ozone depending on leaf age, in the associated damage functions might give a different picture. For herbal

515 and grassland species (similar for crops) a strong dependency on the phenological state, e.g. high susceptibility to ozone in the reproductive state, was found (Bassin et al., 2004).

To estimate potential biases in the assessment of ozone-induced risk on Fennoscandic vegetation, we defined hypothetical temperature response functions representing different levels of assumed acclimation to cold climates. We assume northern Fennoscandia vegetation to be more tolerant towards cold temperatures and less tolerant to heat. Based on probability density functions (PDF) of observed light and temperature, we assume that an acclimation ought to increase the enclosed area between the respective response functions and the PDF. These hypothetical parameterisations of species or PFTs still need verification by experimental data.

In summary, our key findings are:

- 525 1. the bespoke parameterizations for subarctic species are important (especially concerning light and temperature and the climate effect on the growing season) to be able to assess O₃ uptake,
2. the parameterizations defined in the mapping manual for European regional risk assessment appear to not adequately capture the physiological responses of subarctic physiology that are important determinants of [O₃] sensitivity and are likely to substantially underestimate risk,
3. the ozone reanalysis products tend to underestimate [O₃] in Fennoscandia, and
- 530 4. that the climatic conditions promoting ozone damage (particularly extended heatwaves and the timing of the growing season concerning the ozone spring peak) and which are likely to become more frequent under climate change are likely to further enhance the sensitivity of subarctic vegetation to ozone.

However, the decline of the ozone spring peak is partly caused by dry deposition of ozone on vegetation. It, therefore, remains unclear whether an earlier start of the growing season has the potential to reduce the ozone spring peak concentration 535 compared to present-day and hence reduce the damage risk of ozone in the future. We have not assessed the effect of the plants' response to VPD here, but our climatological data show that conditions at Svanhovd are shifting towards a more VPD limited regime.

Based on the methods described in Mills et al. (2017), we estimated biomass reductions due to ozone uptake for both 2018 and 2019 and found significant reductions for deciduous trees (15.5 – 17.4 %) and perennial grassland (above ground, 540 12.4 – 13.7 %) with respect to estimates based on POD₁ from default parameterizations. For coniferous trees, the adjusted parameterizations are comparable with the default parameterization estimates and are contained within the range of systematic uncertainties deduced from our bespoke response function (2.5 – 3 %). These results have to be treated with care because the biomass reduction functions were not established based on subarctic species.

At the same time, intra-species variability even at the same location is typically non-negligible (Bassin et al., 2004; Girgždienė et al., 2009). This may explain contradictory results regarding the ozone sensitivity of natural vegetation in northern Europe. While Subramanian et al. (2014) reported a modeled reduction of net primary production in coniferous (4.3 – 15.5 %) and birch (1.4 – 4.3 %) under elevated ozone in Sweden, Lithuanian forest deciduous trees were observed to be more susceptible to visible damage by ozone than Norway spruce (Girgždienė et al., 2009). Open-top chamber (OTC) experiments performed

in northern Finland where Scots pine and downy birch were exposed to elevated ozone concentrations showed biomass reductions of both downy birch and mountain birch seedlings after one season of exposure (Manninen et al., 2009). The leaves of the mountain birch in the high ozone treatments showed necrotic stipules as early as June. As mountain birch very rapidly develops during spring and early summer, compensation for damaged leaves is difficult for this species. In contrast to mountain birches, northern Scots pine of local origin only showed invisible needle-level O₃ impacts after three years of exposure. There is no field data comparing the ozone sensitivity of birches and Scots pine from northern Europe. In our study, we do not explicitly account for this natural distribution of individual plant traits, but the chosen hypothetical, bespoke response functions might reflect this diversity within a given species or PFT. The resilience of northern Fennoscandia plant communities to climate change and predictions in this regard strongly depends on both the existing range of acclimations as well as the actual type of acclimation.

Cumulative ozone uptake has been reported to reduce stomatal conductance significantly and independently from photosynthesis (Lombardozzi et al., 2012, e.g.), with photosynthesis being more strongly affected. This might be due to competing effects, as an ozone-induced sluggishness (Hoshika et al., 2015) renders stomata unable to fully close and leads to higher stomatal conductance than expected and thus higher ozone uptake as well as transpiration. At present, the MM version of the DO₃SE model does not account for any ozone-inflicted reduction of stomatal conductance throughout the growing season and is not coupled to photosynthesis. Hence, the presented POD_y may be regarded as an estimated upper limit.

565

Beyond the risk assessment of ozone-induced damage, our hypothetical bespoke temperature response functions, once verified by observations, can have important implications on land-surface modeling in global models, where problems in productivity of species especially in the Arctic regions occur due to PFTs which are not suitable for the climate. We pointed out, with respect to default perennial grassland parameterization, that these perennial grasslands did not show any substantial stomatal conductance in 2019 characterized as a normal year. In terms of GPP this would mean unrealistically low carbon sequestration. Automation of the here proposed PDF-based acclimation using machine learning techniques could overcome these issues in the future.

Data availability. All data is available from public databases or through institutional access. DO₃SE modeling results can be made available upon request **TODO: Upload to an achieve together with processed, gap filled input data on zenodo?.**

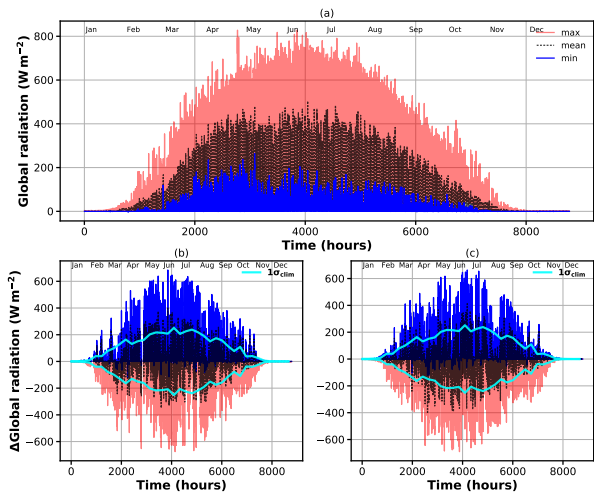


Figure A1. Observed global irradiance at Svanvik. (a) Climatology (hourly maxima, mean, and minima); deviation from climatology (b) 2018; (c) 2019. The cyan lines indicate the 1σ level derived from climatology.

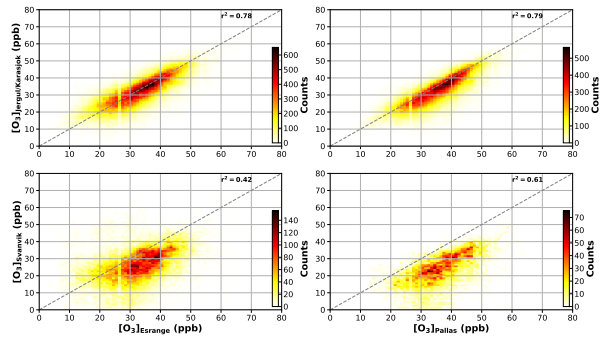


Figure A2. Probability densities and correlation coefficient for $[O_3]$ between different sites in northern Fennoscandia. Jergul/Karasjok is well correlated with Esrange, and Pallas. Svanvik displays highest correlation with Pallas. Note: The stripe at 26 ppb is an artifact from plotting. (a) Jergul/Karasjok–Esrange; (b) Jergul/Karasjok–Pallas; (c) Svanvik–Esrange; (d) Svanvik–Pallas.

Appendix B: DO3SE model

B1 Model description

The opening of stomata is governed by different species-specific and environmental factors and can be described by a multiplicative model (Jarvis, 1976; Emberson et al., 2000; Mills et al., 2017):

$$580 \quad g_{\text{sto}}^k = g_{\max}^k \cdot f_{\text{phen}}^k \cdot f_{\text{light}}^k \cdot \max \{ f_{\min}^k, f_T^k \cdot f_{\text{VPD}}^k \cdot f_{\text{SWP}}^k \}. \quad (\text{B1})$$

Where g_{\max} is the specific-specific maximum stomatal conductance value which is then modified by seasonal and environmental factors that vary within a range 0 – 1. They are empirically determined and account for leaf phenology (f_{phen}), light (f_{light}), temperature (f_T), water vapor pressure deficit (f_{VPD}), and soil water potential (f_{SWP}). All factors differ with species or plant functional type (PFT) denoted with k .

585 The temperature adjustment function is defined as

$$f_T = \frac{T_{\text{air}} - T_{\min}}{T_{\text{opt}} - T_{\min}} \cdot \left(\frac{T_{\max} - T_{\text{air}}}{T_{\max} - T_{\text{opt}}} \right)^{\beta}, \quad (\text{B2})$$

with $\beta = \frac{T_{\max} - T_{\text{opt}}}{T_{\text{opt}} - T_{\min}}$ a mixed reciprocal polynomial function of temperature. The shape parameters T_{\min} , T_{\max} and T_{opt} are tabulated for various species or PFT and T_{air} is the near-surface air temperature. All temperatures are defined in units of °C.

The water vapor pressure deficit function is

$$590 \quad f_{\text{VPD}} = f_{\min} + (1 - f_{\min}) \cdot \frac{D_{\min} - \text{VPD}}{D_{\min} - D_{\max}} \quad (\text{B3})$$

where VPD is the leaf to air vapor pressure deficit in kPa with f_{\min} , D_{\min} , D_{\max} describing the relative stomatal conductance to changes in vapor pressure deficit.

The wavelength band 400 – 700 nm plant chlorophyll responds to is called photosynthetic active radiation (PAR). Its integral is the photosynthetic photon flux density (PPFD). The relationship between relative g_{sto} and PPFD is given by

$$595 \quad f_{\text{light}} = 1 - \exp(-\alpha_{\text{light}} \cdot \text{PPFD}) \quad (\text{B4})$$

where α_{light} is a slope parameter describing the extent of stomatal opening at low light intensities.

The DO₃SE model as described in Büker et al. (2012) is used to simulate SWP across a species or PFT specific root depth according to the Penman–Monteith energy balance method that drives water cycling through the soil–plant–atmosphere system. Büker et al. (2012) discuss several formulations available to parameterize the reduction in stomata conductance due to water content in the soil. Here we use the relationship between relative g_{sto} and soil water potential (SWP) given by:

$$600 \quad f_{\text{SWP}} = \min \left\{ 1, \max \left\{ f_{\min}, \frac{(1 - f_{\min}) \cdot (\text{SWP}_{\min} - \text{SWP})}{\text{SWP}_{\min} - \text{SWP}_{\max}} + f_{\min} \right\} \right\} \quad (\text{B5})$$

where SWP is the soil water potential across the root zone and SWP_{\min} and SWP_{\max} are the parameters describing the f_{SWP} relationship.

To compute POD_y , we estimate the stomatal O₃ flux (Φ_{sto}) based on the assumption that the concentration of O₃ at the top of the canopy represents a reasonable estimate of the concentration at the upper surface of the laminar layer for a sunlit upper canopy leaf. The terms r_c (leaf surface resistance) and r_b (quasi-laminar resistance) allow for the deposition of O₃ to the leaf and the fraction that is taken up via the stomata.

$$\Phi_{\text{sto}} = [\text{O}_3] \cdot \frac{u(z_1) \cdot g_{\text{sto}} \cdot r_c}{r_b + r_c}. \quad (\text{B6})$$

The quasi-laminar boundary layer resistance is calculated by

$$r_b = 1.3 \cdot 150 \cdot \sqrt{\frac{L}{u(z_1)}}. \quad (\text{B7})$$

Where L is the cross-wind leaf dimension, $u(z_1)$ the wind speed at height z_1 , and the factor 1.3 accounts for the diffusivity between heat and O₃.

B2 Input data and gap filling methodology

The DO₃SE model requires hourly, continuous meteorological observations. In addition to variables covered in Section 2, 2m wind $u_{2\text{m}}$ and vapor pressure deficit VPD are needed. VPD has been calculated from observed $T_{2\text{m}}$ and relative humidity

$$\text{VPD} = P_s(T) \cdot \left(1 - \frac{\text{relHum}}{100}\right), \quad (\text{B8})$$

with saturation vapor pressure $P_s(T)$ in hPa derived from Arden Buck equation (Buck, 1981; Buck Research Instruments, LLC, 2012).

The following gap filling methodology was devised for the meteorological input data:

- Single hours of missing data were filled by taking the average of the hourly values coming before, and after, the missing value.
- Several consecutive hours of missing data (23 or less) were filled by taking the average of the corresponding hour the day before, and the day after; and repeating this for each missing hour of data. If data were unavailable from that hour of the previous day, then only the value from the day after was used and vice versa. Interpolated values were not used in calculating averages.
- Data gaps longer than 24h were filled using weekly diurnal averages. i.e. an average was calculated using the corresponding hour throughout the week before and after. Interpolated values were not used in calculating averages.

For the missing ozone data, we applied a Reynolds decomposition of the form:

$$[\text{O}_3] = \langle [\text{O}_3] \rangle + \Delta[\text{O}_3], \quad (\text{B9})$$

with climatology $\langle [\text{O}_3] \rangle$ and anomalies $\Delta[\text{O}_3]$. Observed [O₃] in 2018 at Pallas served as the reference. The exact procedure will be described in an companion paper.

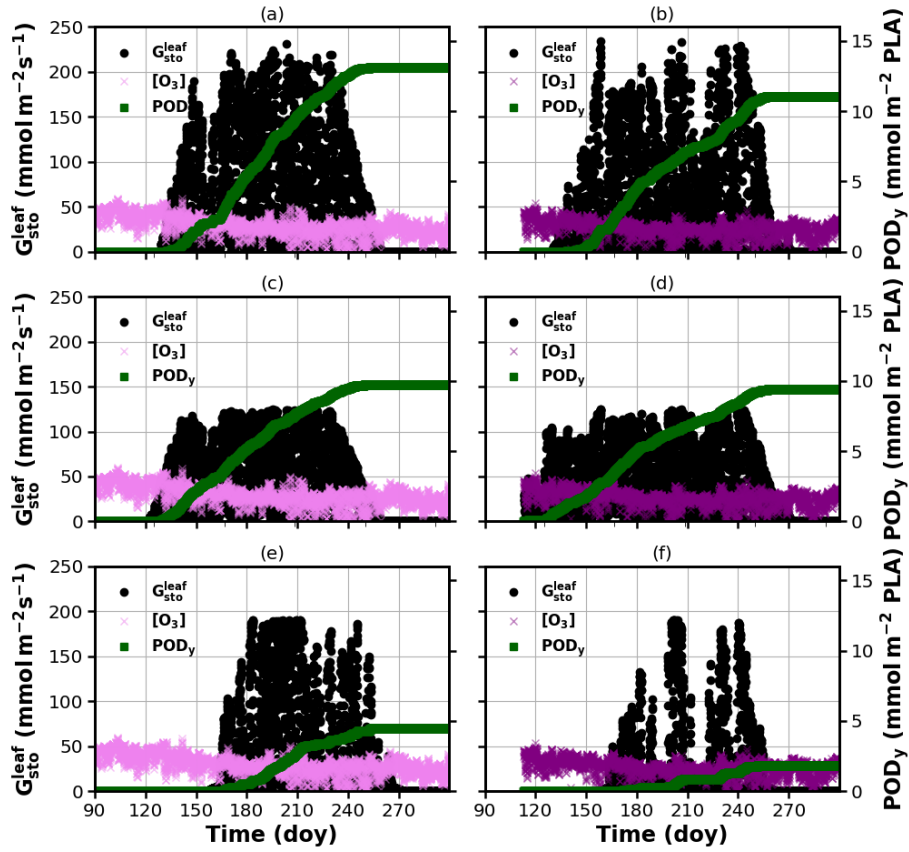


Figure B1. DO₃SE modeling results for mapping manual default parameterization. POD_y is shown over day of year (doy), March–October. A flux threshold $y = 1 \text{ nmol m}^{-2} \text{ s}^{-1}$ per projected leaf area (PLA) has been chosen. [O₃] is plotted on the same axis and scales as $G_{\text{sto}}^{\text{leaf}}$ but in units of ppb. (a, b) deciduous tree; (c, d) coniferous tree; (e, f) perennial grassland. From left to right: 2018, 2019.

B3 Initial DO₃SE modeling results with mapping manual parameters

To demonstrate the necessity of acclimation from the mapping manual parameters, we show the initial results of stomatal conductance at leaf-level ($G_{\text{sto}}^{\text{leaf}}$) and POD_y over doy for both years and all species or PFTs (Fig. B1). Observed [O₃] is also indicated. From Fig. B1f) and the assumption of a linear relationship between An and Gsto (Medlyn, xxx) it is apparent that the mapping manual parameterized grassland would not have been able to grow in 2019, which is not a realistic result.

B4 Bespoke parameterizations

To assess the G_{start} and G_{end} of the growing season for coniferous trees at Svanhovd in 2018/19, we used the net photosynthesis product (A_{net}) of MODIS AQUA/TERRA over a $1 \times 1 \text{ km}$ area centered at Svanhovd. MODIS data indicate a higher

640 photosynthetic activity in 2018 than in 2019. As shown in Fig. B2 we fitted a second order polynomial function of the general form

$$A_{\text{net}}(t) = -m_0 \cdot (t - m_1)^2 + m_2, \quad (\text{B10})$$

with the form parameters m_i through the data. Numerically, we retrieved the roots as G_{start} 122/106 and G_{end} 261/274 for 2018 and 2019, respectively.

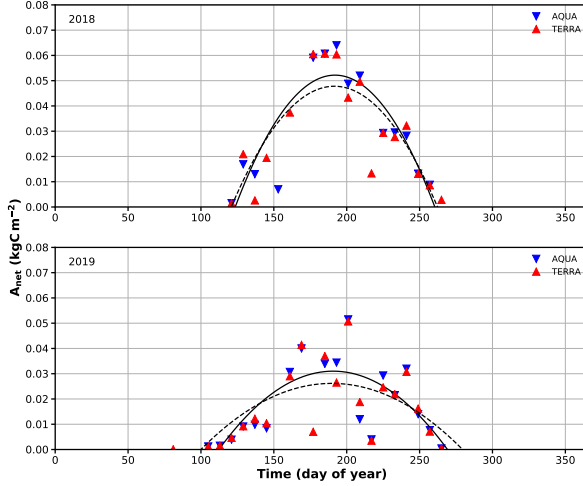


Figure B2. Estimated G_{start} and G_{end} of growing season for coniferous trees from MODIS Aqua/Terra net photosynthesis (PSN) product. A 1×1 km area around Svanhovd was selected. Daily averaged data for both 2018 and 2019 has been fitted with a quadratic polynomial function. The numerically computed root yields: BGS 122/106 day of year (doy) and EGS 261/274 day of year for 2018/2019, respectively.

645 As described in Section 4.1, we developed bespoke parameterizations for natural and semi-natural vegetation at Svanhovd. Here, we show the temperature response and light response functions for coniferous and deciduous trees (Figs. B3-B4).

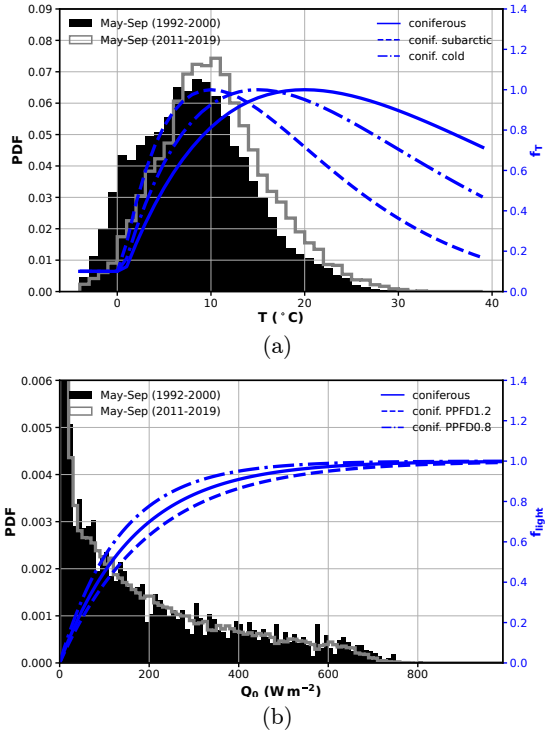


Figure B3. Construction of bespoke response functions for coniferous trees. (a) f_T and (b) f_{light} are shown together with underlying T_{air} and Q_0 climatologies (probability density function - PDF), respectively. Original mapping manual parameterization is shown in comparison as solid line. Note that Q_0 has been truncated to 0.006. PPFD0.8 and PPFD1.2 refer to α values increasing/decreasing PPFD at $f_{\text{light}} = 0.5$ by $\pm 20\%$, respectively.

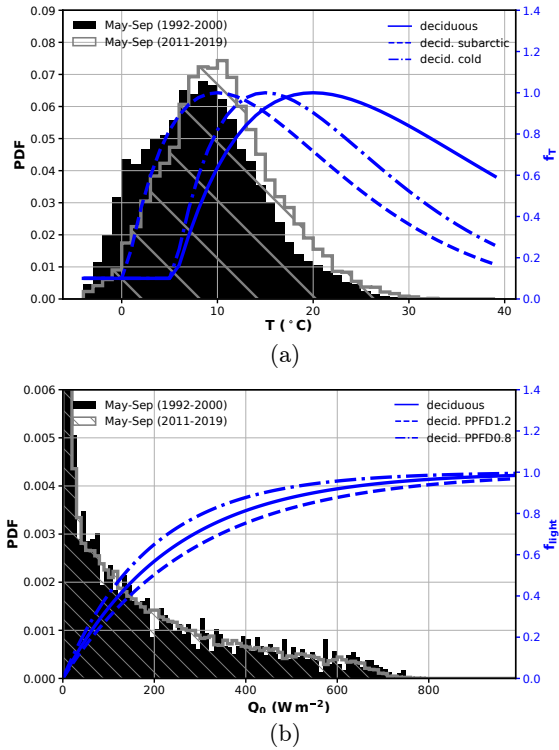


Figure B4. Construction of bespoke response functions for deciduous trees. (a) f_T and (b) f_{flight} are shown together with underlying T_{air} and Q_0 climatologies (probability density function - PDF), respectively. Original mapping manual parameterization is shown in comparison as solid line. Note that Q_0 has been truncated to 0.006. PPFD0.8 and PPFD1.2 refer to α values increasing/decreasing PPFD at $f_{\text{flight}} = 0.5$ by $\pm 20\%$, respectively.

Author contributions. SF has written the manuscript, collected and processed ozone and environmental data, and performed all statistical analyses. AVV contributed to framing this research article, has performed the on-site observation of vegetation damage induced by ozone, and advising in plant physiological processes. LE has contributed to framing of the this article, DO₃SE modeling, and development of the PDF-based temperature acclimation. CO has collected species or PFT parameters from literature, performed all DO₃SE simulations and initial validation of the results. AE contributed with her experience regarding subarctic vegetation in Finnmark. FS contributed with an assessment of the 2018 meteorological conditions. TB gave guidance in a broader research sense. All authors contributed to discussions, writing, and conclusions.

Competing interests. The authors declare that they have no conflict of interest.

Acknowledgements. Bjørg Rognerud for processing SeNorge.no data with respect for begin of growing season. Tore Flatlandsmo Berglen for hourly pressure data from Svanhovd. This work was financed by the Research Council of Norway (NRC) grand No. 268073.

References

- Ainsworth, E. A.: Understanding and improving global crop response to ozone pollution, *Plant J.*, 90, 886–897, <https://doi.org/10.1111/tpj.13298>, 2017.
- 660 AMAP - Arctic Monitoring and Assessment Programme: Arctic Climate Issues 2011: Changes in Arctic Snow, Water, Ice and Permafrost, SWIPA 2011 Overview Report, Oslo, 978-82-7971-073-8, 2012.
- Andersson, C., Alpfjord, H., Robertson, L., Karlsson, P. E., and Engardt, M.: Reanalysis of and attribution to near-surface ozone concentrations in Sweden during 1990–2013, *Atmospheric Chemistry and Physics*, 17, 13 869–13 890, <https://doi.org/10.5194/acp-17-13869-2017>, 2017.
- 665 Ball, J., Woodrow, I., and Berry, J.: Progress in Photosynthesis Research, chap. A Model Predicting Stomatal Conductance and its Contribution to the Control of Photosynthesis under Different Environmental Conditions, Springer, Dordrecht, https://doi.org/10.1007/978-94-017-0519-6_48, 1987.
- Bassin, S., Kölliker, R., Cretton, C., Bertossa, M., Widmer, F., Bungener, P., and Fuhrer, J.: Intra-specific variability of ozone sensitivity in *Centaurea jacea* L., a potential bioindicator for elevated ozone concentrations, *Environ. Pollut.*, 131, 1–12, 670 <https://doi.org/10.1016/j.envpol.2004.02.014>, 2004.
- Beck, H., Zimmermann, N., McVicar, T., Vergopolan, N., Berg, A., and Wood, E.: Present and future Köppen-Geiger climate classification maps at 1-km resolution, *Sci. Data*, 5, 180 214, <https://doi.org/10.1038/sdata.2018.214>, 2018.
- Björklund, J.-Å., Ekelund, K., Henningsson, A., Perers, K., Peters, J., Siverstig, A., Uddholm, L.-G., and Wisén, J.: Betänkande av 2018 års skogsbrandsutredning, SOU2019 7, Statens Offentliga Utredningar (SOU), <https://www.regeringen.se/rattsliga-dokument/statens-offentliga-utredningar/2019/02/sou-20197/>, 2019.
- 675 Buck, A. L.: New Equations for Computing Vapor Pressure and Enhancement Factor, *J. Appl. Meteorol.*, 20, 1527–1532, [https://doi.org/10.1175/1520-0450\(1981\)020<1527:NEFCVP>2.0.CO;2](https://doi.org/10.1175/1520-0450(1981)020<1527:NEFCVP>2.0.CO;2), 1981.
- Buck Research Instruments, LLC: Buck Research CR-1A User's Manual, Buck Research Instruments, LLC, PO Box 19498 Boulder, CO 80308, Appendix 1, 2012.
- 680 Büker, P., Morrissey, T., Briolat, A., Falk, R., Simpson, D., Tuovinen, J.-P., Alonso, R., Barth, S., Baumgarten, M., Grulke, N., Karlsson, P., King, J., Lagergren, F., Matyssek, R., Nunn, A., Ogaya, R., Penuelas, J., Rhea, L., Schaub, M., and Emberson, L.: DO3SE modelling of soil moisture to determine ozone flux to European forest trees, *Atmos. Chem. Phys.*, 12, 5537–5562, <https://doi.org/10.5194/acp-12-5537-2012>, 2012.
- Chuwah, C., van Noije, T., van Vuuren, D. P., Stehfest, E., and Hazeleger, W.: Global impacts of surface ozone changes on crop yields and land use, *Atmos. Environ.*, 106, 11–23, <https://doi.org/10.1016/j.atmosenv.2015.01.062>, 2015.
- 685 Clifton, O., Fiore, A., Massman, W., Baublitz, C., Coyle, M., Emberson, L., Fares, S., Farmer, D., Gentine, P., Gerosa, G., Guenther, A., Helmig, D., Lombardozzi, D., Munger, J., Patton, E., Pusede, S., Schwede, D., Silva, S., Sörgel, M., and Tai, A.: Dry Deposition of Ozone Over Land: Processes, Measurement, and Modeling, *Reviews of Geophysics*, p. e2019RG000670, <https://doi.org/10.1029/2019RG000670>, 2020.
- 690 Cofer, W. R., Levine, J. S., Winstead, E. L., and Stocks, B. J.: Gaseous emissions from Canadian boreal forest fires, *Atmos. Environ.*, 24, 1653–1659, [https://doi.org/10.1016/0960-1686\(90\)90499-D](https://doi.org/10.1016/0960-1686(90)90499-D), 1990.

- Cooper, O., Parrish, D., Ziemke, J., Balashov, N., Cupeiro, M., Galbally, I., Gilge, S., Horowitz, L., Jensen, N., Lamarque, J.-F., Naik, V., Oltmans, S., Schwab, J., Shindell, D., Thompson, A., Thouret, V., Wang, Y., and Zbinden, R.: Global distribution and trends of tropospheric ozone: An observation-based review, *Elementa-Sci Anthropol.*, 2, 000 029, <https://doi.org/10.12952/journal.elementa.000029>, 2014.
- 695 Derwent, R. G., Parrish, D. D., Galbally, I. E., Stevenson, D. S., Doherty, R. M., Naik, V., and Young, P. J.: Uncertainties in models of tropospheric ozone based on Monte Carlo analysis: Tropospheric ozone burdens, atmospheric lifetimes and surface distributions, *Atmos. Environ.*, 180, 93–102, <https://doi.org/10.1016/j.atmosenv.2018.02.047>, 2018.
- DSB: Skogbrannsesongen 2018 – Erfaringer og læringspunkter, Report 2402, Direktoratet for samfunnssikkerhet og beredskap (DSB), <https://www.dsbs.no/rapporter-og-evalueringer/skogbrannsesongen-2018/>, 2019.
- 700 Emberson, L.: Effects of ozone on agriculture, forests and grasslands, *Philosophical transactions. Series A, Mathematical, physical, and engineering sciences*, 378, 20190 327, <https://doi.org/10.1098/rsta.2019.0327>, 2020.
- Emberson, L. D., for Monitoring, C. P., of the Long Range Transmission of Air Pollutants in Europe, E., meteorologiske institutt, N., and Meteorological Synthesizing Centre-West (Oslo, N.: Towards a Model of Ozone Deposition and Stomatal Uptake Over Europe, EMEP/MSC-W Note, Norwegian Meteorological Institute, https://books.google.no/books?id=hj_ntgAACAAJ, 2000.
- 705 Fleming, Z. L., Doherty, R. M., von Schneidemesser, E., Malley, C. S., Cooper, O. R., Pinto, J. P., Colette, A., Xu, X., Simpson, D., Schultz, M. G., Lefohn, A. S., Hamad, S., Moolla, R., Solberg, S., and Feng, Z.: Tropospheric Ozone Assessment Report: Present-day ozone distribution and trends relevant to human health, *Elementa-Sci Anthropol.*, 6, <https://doi.org/10.1525/elementa.273>, 2018.
- Galbally, I. and Roy, C.: Destruction of ozone at the earth's surface, *Q. J. Roy. Meteorol. Soc.*, 106, 599–620, <https://doi.org/10.1002/qj.49710644915>, 2007.
- 710 Gangstø Skaland, R., Colleuille, H., Håvelsrød Andersen, A. S., Mamen, J., Grinde, L., Tajet, H. T. T., Lundstad, E., Sidselrud, L. F., Tunheim, K., Hanssen-Bauer, I., Benestad, R., Heiberg, H., and Hygen, H. O.: Tørkesommeren 2018, METinfo 14, Norwegian Meteorological Institute, <https://www.met.no/publikasjoner/met-info/met-info-2019>, 2019.
- Gaudel, A., Cooper, O. R., Ancellet, G., Barret, B., Boynard, A., Burrows, J. P., Clerbaux, C., Coheur, P. F., Cuesta, J., Cuevas, E., Doniki, S., Dufour, G., Ebojie, F., Foret, G., Garcia, O., Granados-Munoz, M. J., Hannigan, J. W., Hase, F., Hassler, B., Huang, G., Hurtmans, 715 D., Jaffe, D., Jones, N., Kalabokas, P., Kerridge, B., Kulawik, S., Latter, B., Leblanc, T., Le Flochmoen, E., Lin, W., Liu, J., Liu, X., Mahieu, E., McClure-Begley, A., Neu, J. L., Osman, M., Palm, M., Petetin, H., Petropavlovskikh, I., Querel, R., Rahpoe, N., Rozanov, A., Schultz, M. G., Schwab, J., Siddans, R., Smale, D., Steinbacher, M., Tanimoto, H., Tarasick, D. W., Thouret, V., Thompson, A. M., Trickl, T., Weatherhead, E., Wespes, C., Worden, H. M., Vigouroux, C., Xu, X., Zeng, G., and Ziemke, J.: Tropospheric Ozone Assessment Report: Present-day distribution and trends of tropospheric ozone relevant to climate and global atmospheric chemistry model evaluation, *Elementa-Sci Anthropol.*, 6, <https://doi.org/10.1525/elementa.291>, 2018.
- 720 Girgždienė, R., Serafinavičiūtė, B., Stakėnas, V., and Byčenkiė, S.: Ambient Ozone Concentration and its Impact on Forest Vegetation in Lithuania, *AMBIO A Journal of the Human Environment*, pp. 432–436, <https://doi.org/10.1579/0044-7447-38.8.432>, 2009.
- Hatakka, J., Aalto, T., Aaltonen, V., Aurela, M., Hakola, H., Komppula, M., Laurila, T., Lihavainen, H., Paatero, J., Salminen, K., and Viisanen, Y.: Overview of the atmospheric research activities and results at Pallas GAW station, *Boreal Environ. Res.*, 8, 365–383, 2003.
- 725 Hayes, F., Harmens, H., Mills, G., Bender, J., and Grünhage, L.: Ozone critical levels for (semi-)natural vegetation dominated by perennial grassland species, *Environ. Sci. Pollut. Res.*, 28, 15 090–15 098, <https://doi.org/10.1007/s11356-020-11724-w>, 2021.
- Helming, D., Ganzeveld, L., Butler, T., and Oltmans, S. J.: The role of ozone atmosphere-snow gas exchange on polar, boundary-layer tropospheric ozone - a review and sensitivity analysis, *Atmos. Chem. Phys.*, 7, 2007.

- Høgda, K., Tømmervik, H., and Karlsen, S.: Trends in the Start of the Growing Season in Fennoscandia 1982–2011, *Remote Sens.*, 5, 4304–4318, <https://doi.org/10.3390/rs5094304>, 2013.
- 730 Hoshika, Y., Katata, G., Deushi, M., Watanabe, M., Koike, T., and Paoletti, E.: Ozone-induced stomatal sluggishness changes carbon and water balance of temperate deciduous forests, *Sci. Rep.-UK*, 5, <https://doi.org/10.1038/srep09871>, 2015.
- IPCC - Intergovernmental Panel on Climate Change: Climate Change 2013: The Physical Science Basis, 2013.
- Jarvis, P. G.: The interpretation of the variations in leaf water potential and stomatal conductance found in canopies in the field, *Philos. T. Roy. Soc. B.*, 273, 593–610, <https://doi.org/10.1098/rstb.1976.0035>, 1976.
- 735 Juran, S., Edwards-Jonášová, M., Cudlín, P., Zapletal, M., Sigut, L., Grace, J., and Urban, O.: Prediction of ozone effects on net ecosystem production of Norway spruce forest, *iForest - Biogeosciences and Forestry*, 11, 743–750, <https://doi.org/10.3832/ifor2805-011>, 2018.
- Kangaskärvi, J., Jaspers, P., and Kollist, H.: Signalling and cell death in ozone-exposed plants, *Plant, Cell & Environment*, 28, 1021–1036, <https://doi.org/10.1111/j.1365-3040.2005.01325.x>, 2005.
- 740 Karlsen, S., Solheim, I., Beck, P., Høgda, K., Wielgolaski, F., and Tømmervik, H.: Variability of the start of the growing season in Fennoscandia, 1982–2002, *Int. J. Biometeorol.*, 51, 513–24, <https://doi.org/10.1007/s00484-007-0091-x>, 2007.
- Karlsson, P., Ferm, M., Tømmervik, H., Hole, L., Karlsson, G., Ruoho-Airola, T., Aas, W., Hellsten, S., Akselsson, C., Mikkelsen, T., and Nihlgård, B.: Biomass burning in eastern Europe during spring 2006 caused high deposition of ammonium in northern Fennoscandia, *Environ. Pollut.*, 176C, 71–79, <https://doi.org/10.1016/j.envpol.2012.12.006>, 2013.
- 745 Karlsson, P. E., Pihl Karlsson, G., and Pleijel, H.: En förbättrad metodik för att beräkna ozonkänsliga perioder för växtligheten under året, Tech. rep., IVL Svenska Miljöinstitutet, <https://gup.ub.gu.se/publication/273605>, 2018.
- Klingberg, J., Björkman, M., Karlsson, G., and Pleijel, H.: Observations of Ground-level Ozone and NO₂ in Northernmost Sweden, Including the Scandian Mountain Range, *AMBIO*, 38, 448–451, <https://doi.org/10.1579/0044-7447-38.8.448>, 2009.
- 750 Klingberg, J., Karlsson, P. E., Andersson, C., Engardt, M., Karlsson, G. P., and Pleijel, H.: Observed annual surface ozone maxima and minima in northern and central Europe from 1990–2015 – latitude dependence and temporal trends, *Boreal Environ. Res.*, 24, 201–214, 2019.
- Kolari, P., Lappalainen, H., Hänninen, H., and Hari, P.: Relationship between temperature and the seasonal course of photosynthesis in Scots pine at northern timberline and in southern boreal zone, *Tellus B*, 59, 542–552, <https://doi.org/10.3402/tellusb.v59i3.17033>, 2007.
- Laurila, T. and Hakola, H.: Seasonal cycle of C₂–C₅ hydrocarbons over the Baltic Sea and Northern Finland, *Atmos. Environ.*, 30, 1597–1607, [https://doi.org/10.1016/1352-2310\(95\)00482-3](https://doi.org/10.1016/1352-2310(95)00482-3), Joint 8th CAGCP and 2nd IGAC Conference on Global Atmospheric Chemistry, 1996.
- 755 Lawrence, D. M., Fisher, R. A., Koven, C. D., Oleson, K. W., Swenson, S. C., Bonan, G., Collier, N., Ghimire, B., van Kampenhout, L., Kennedy, D., Kluzek, E., Lawrence, P. J., Li, F., Li, H., Lombardozzi, D., Riley, W. J., Sacks, W. J., Shi, M., Vertenstein, M., Wieder, W. R., Xu, C., Ali, A. A., Badger, A. M., Bisht, G., van den Broeke, M., Brunke, M. A., Burns, S. P., Buzan, J., Clark, M., Craig, A., Dahlin, K., Drewniak, B., Fisher, J. B., Flanner, M., Fox, A. M., Gentine, P., Hoffman, F., Keppel-Aleks, G., Knox, R., Kumar, S., Lenaerts, J., Leung, L. R., Lipscomb, W. H., Lu, Y., Pandey, A., Pelletier, J. D., Perket, J., Randerson, J. T., Ricciuto, D. M., Sanderson, B. M., Slater, A., Subin, Z. M., Tang, J., Thomas, R. Q., Val Martin, M., and Zeng, X.: The Community Land Model Version 5: Description of New Features, Benchmarking, and Impact of Forcing Uncertainty, *J. Adv. Model. Earth Syst.*, 11, 4245–4287, <https://doi.org/10.1029/2018MS001583>, 2019.

- 765 Lin, M., Horowitz, L., Xie, Y., Paulot, F., Malyshev, S., Shevliakova, E., Finco, A., Gerosa, G., Kubistin, D., and Pilegaard, K.: Vegetation feedbacks during drought exacerbate ozone air pollution extremes in Europe, *Nat. Clim. Change*, 10, 444–451, <https://doi.org/10.1038/s41558-020-0743-y>, 2020.
- Lindskog, A., Karlsson, P., Grennfelt, P., Solberg, S., and Forster, C.: An exceptional ozone episode in northern Fennoscandia, *Atmos. Environ.*, 41, 950–958, <https://doi.org/10.1016/j.atmosenv.2006.09.027>, 2007.
- 770 Lombardozzi, D., Levis, S., Bonan, G., and Sparks, J. P.: Predicting photosynthesis and transpiration responses to ozone: decoupling modeled photosynthesis and stomatal conductance, *Biogeosciences*, 9, 3113–3130, <https://doi.org/10.5194/bg-9-3113-2012>, 2012.
- Maas, R., grennfelt, p., Amann, M., Harnett, B., Kerr, J., Berton, E., Pritula, D., Reiss, I., Almodovar, P., Héroux, M.-E., Fowler, D., Wright, D., de Wit, H., Tørseth, K., Mareckova, K., LeGall, A.-C., Rabago, I., Hettelingh, J.-P., Haeuber, R., and Reis, S.: Towards Cleaner Air. Scientific Assessment Report 2016, UN ECE, 2016.
- 775 Manninen, S., Huttunen, S., Tømmervik, H., Hole, L. R., and Solberg, S.: Northern Plants and Ozone, *AMBIO: A Journal of the Human Environment*, 38, 406 – 413, <https://doi.org/10.1579/0044-7447-38.8.406>, 2009.
- Matyssek, R., Wieser, G., Calfapietra, C., de Vries, W., Dizengremel, P., Ernst, D., Jolivet, Y., Mikkelsen, T. N., Mohren, G. M. J., Le Thiec, D., Tuovinen, J. P., Weatherall, A., and Paoletti, E.: Forests under climate change and air pollution: Gaps in understanding and future directions for research, *Environ. Pollut.*, 160, 57–65, <https://doi.org/10.1016/j.envpol.2011.07.007>, 2012.
- 780 Medlyn, B. E., Duursma, R. A., Eamus, D., Ellsworth, D. S., Prentice, I. C., Barton, C. V. M., Crous, K. Y., de Angelis, P., Freeman, M., and Wingate, L.: Reconciling the optimal and empirical approaches to modelling stomatal conductance, *Glob. Change Biol.*, 17, 2134–2144, <https://doi.org/10.1111/j.1365-2486.2010.02375.x>, 2011.
- Menzel, A., Sparks, T., Estrella, N., Koch, E., Aasa, A., Ahas, R., Alm-Kübler, K., Bissolli, P., Braslavská, O., Briede, A., Chmielewski, F., Črepinské, Z., Curnel, Y., Defila, C., Donnelly, A., Filella, I., Jatczak, K., Måge, F., and Zist, A.: European phenological response to climate change matches the warming pattern, *Glob. Change Biol.*, 12, 1969–1976, <https://doi.org/10.1111/j.1365-2486.2006.01193.x>, 2006.
- 785 Mills, G., Hayes, F., Simpson, D., Emberson, L., Norris, D., Harmens, H., and Büker, P.: Evidence of widespread effects of ozone on crops and (semi-)natural vegetation in Europe (1990–2006) in relation to AOT40- and flux-based risk maps, *Glob. Change Biol.*, 17, 592 – 613, <https://doi.org/10.1111/j.1365-2486.2010.02217.x>, 2011.
- 790 Mills, G., Sharps, K., Simpson, D., Pleijel, H., Broberg, M., Uddling, J., Jaramillo, F., Davies, W. J., Dentener, F., Van den Berg, M., Agrawal, M., Agrawal, S. B., Ainsworth, E. A., Büker, P., Emberson, L., Feng, Z., Harmens, H., Hayes, F., Kobayashi, K., Paoletti, E., and Van Dingenen, R.: Ozone pollution will compromise efforts to increase global wheat production, *Glob. Change Biol.*, 24, 3560–3574, <https://doi.org/10.1111/gcb.14157>, 2018.
- Mills, G., Harmens, H., Hayes, F., Pleijel, H., Büker, P., González-Fernández, I., Alonso, R., Bender, J., Bergmann, E., Bermejo, V., Braun, S., Danielsson, H., Gerosa, G., Grünhage, L., Karlsson, P. E., Marzuoli, R., Schaub, M., and Simpson, D.: ICP Mapping Manual - Chapter III: Mapping Critical Levels for Vegetation, International Cooperative Programme on Effects of Air Pollution on Natural Vegetation and Crops, https://icpmapping.org/Latest_update_Mapping_Manual, minor edits OCT 2017, 2017.
- 795 Mills, G., Pleijel, H., Malley, C. S., Sinha, B., Cooper, O. R., Schultz, M. G., Neufeld, H. S., Simpson, D., Sharps, K., Feng, Z., Gerosa, G., Harmens, H., Kobayashi, K., Saxena, P., Paoletti, E., Sinha, V., and Xu, X.: Tropospheric Ozone Assessment Report: Present-day tropospheric ozone distribution and trends relevant to vegetation, *Elementa-Sci Anthropol.*, 6, <https://doi.org/10.1525/elementa.302>, 2018.
- Monks, P. S.: A review of the observations and origins of the spring ozone maximum, *Atmos. Environ.*, 34, 3545–3561, [https://doi.org/10.1016/S1352-2310\(00\)00129-1](https://doi.org/10.1016/S1352-2310(00)00129-1), 2000.

- Musselman, R. C., Lefohn, A. S., Massman, W. J., and Heath, R. L.: A critical review and analysis of the use of exposure- and flux-based ozone indices for predicting vegetation effects, *Atmos. Environ.*, 40, 1869–1888, <https://doi.org/10.1016/j.atmosenv.2005.10.064>, 2006.
- 805 NIBIO: LandbruksMeteorologisk Tjeneste, <https://lmt.nibio.no/>, last accessed July 2020, a.
NIBIO: Svanhovd Environment Centre, online, <https://www.nibio.no/en/about-eng/addresses/northern-norway/svanhovd>, last accessed March 2020, b.
NILU: Luftkvalitet.no, online, <http://www.luftkvalitet.no>, last accessed July 2020, a.
NILU: ebas.nilu.no, online, <http://ebas.nilu.no/>, last accessed July 2020, b.
- 810 NVE, Meteorologisk Institutt, Kartverket: SeNorge.no, online, <http://www.senorge.no>, last accessed, 2020.
Peñuelas, J. and Llusia, J.: BVOCs: plant defense against climate warming?, *Trends Plant Sci.*, 8, 105–109, [https://doi.org/10.1016/S1360-1385\(03\)00008-6](https://doi.org/10.1016/S1360-1385(03)00008-6), 2003.
- Poulter, B., MacBean, N., Hartley, A., Khlystova, I., Arino, O., Betts, R., Bontemps, S., Boettcher, M., Brockmann, C., Defourny, P., Hagemann, S., Herold, M., Kirches, G., Lamarche, C., Lederer, D., Ottle, C., Peters, M., and Peylin, P.: Plant functional type classification for 815 earth system models: results from the European Space Agency's Land Cover Climate Change Initiative, *Geosci. Model Dev.*, 8, 2315–2328, <https://doi.org/10.5194/gmd-8-2315-2015>, 2015.
- Rummukainen, M., Laurila, T., and Kivi, R.: Yearly cycle of lower tropospheric ozone at the Arctic Circle, *Atmos. Environ.*, 30, 1875–1885, [https://doi.org/10.1016/1352-2310\(95\)00384-3](https://doi.org/10.1016/1352-2310(95)00384-3), Joint 8th CAGCP and 2nd IGAC Conference on Global Atmospheric Chemistry, 1996.
- 820 Ruoho-Airola, T., Anttila, P., Hakola, H., Ryyppö, T., and Tuovinen, J.-P.: Trends in the bulk deposition and atmospheric concentration of air pollutants in the Finnish Integrated Monitoring catchment Pallas during 1992–2012, *Boreal Environ. Res.*, 20, 553–569, 2015.
- Schnell, R., Oltmans, S., Neely, R., Endres, M., Molenar, J., and White, A.: Rapid photochemical production at high concentrations in a rural site during winter, *Nat. Geosci.*, 2, 120–122, <https://doi.org/10.1038/ngeo415>, 2009.
- Simpson, D., Ashmore, M., Emberson, L., and Tuovinen, J.-P.: A comparison of two different approaches for mapping potential ozone damage to vegetation. A model study, *Environ. Pollut.*, 146, 715–725, <https://doi.org/10.1016/j.envpol.2006.04.013>, critical Levels for 825 Ozone Effects on Vegetation: Further Applying and Developing the Flux Concept, 2007.
- Simpson, W., King, M., Beine, H., A., H., and Peterson, M.: Atmospheric photolysis rate coefficients during the Polar Sunrise Experiment ALERT 2000, *Atmos. Environ.*, 36, 2471–2480, 2002.
- Solberg, S.: Monitoring of boundary layer ozone in Norway from 1977 to 2002, Ozone Report 2003 85, Norwegian Institute for Air Research (NILU), 2003.
- 830 Solberg, S., Hov, Ø., Haslerud, A., Isaksen, S., Coddeville, P., De Backer, H., Forster, C., Orsolini, Y., and Uhse, K.: European surface ozone in the extreme summer 2003, *J. Geophys. Res.*, 113, 1–16, <https://doi.org/10.1029/2007JD009098>, 2008.
- Stevenson, D. S., Dentener, F. J., Schultz, M. G., Ellingsen, K., van Noije, T. P. C., Wild, O., Zeng, G., Amann, M., Atherton, C. S., Bell, N., Bergmann, D. J., Bey, I., Butler, T., Cofala, J., Collins, W. J., Derwent, R. G., Doherty, R. M., Drevet, J., Eskes, H. J., Fiore, A. M., Gauss, M., Hauglustaine, D. A., Horowitz, L. W., Isaksen, I. S. A., Krol, M. C., Lamarque, J.-F., Lawrence, M. G., Montanaro, V., Müller, J.-F., 835 Pitari, G., Prather, M. J., Pyle, J. A., Rast, S., Rodriguez, J. M., Sanderson, M. G., Savage, N. H., Shindell, D. T., Strahan, S. E., Sudo, K., and Szopa, S.: Multimodel ensemble simulations of present-day and near-future tropospheric ozone, *J. Geophys. Res.-Atmos.*, 111, <https://doi.org/10.1029/2005JD006338>, 2005.
- Subramanian, N., Karlsson, P., Bergh, J., and Urban, N.: Impact of Ozone on Sequestration of Carbon by Swedish Forests under a Changing Climate: A Modeling Study, *Forest Science*, 61, <https://doi.org/10.5849/forsci.14-026>, 2014.

- 840 Systad, G. H., Strann, K.-B., and Frivoll, V.: Biologisk mangfold Sør-Varanger kommune, Nina oppdragsmelding, Norsk institutt for naturforskning (NINA), <https://www.nina.no/archive/nina/PppBasePdf/oppdragsmelding/829.pdf>, 2004.
- Tai, A. P. K., Martin, M. V., and Heald, C. L.: Threat to future global food security from climate change and ozone air pollution, *Nat. Clim. Change*, 4, 817–821, <https://doi.org/10.1038/NCLIMATE2317>, 2014.
- Tang, H., Takigawa, M., Liu, G., Zhu, J., and Kobayashi, K.: A projection of ozone-induced wheat production loss in China
845 and India for the years 2000 and 2020 with exposure-based and flux-based approaches, *Glob. Change Biol.*, 19, 2739–2752, <https://doi.org/10.1111/gcb.12252>, 2013.
- Škerlak, B., Sprenger, M., Pfahl, S., Tyrlis, E., and Wernli, H.: Tropopause folds in ERA-Interim: Global climatology and relation to extreme weather events, *J. Geophys. Res.-Atmos.*, 120, 4860–4877, <https://doi.org/10.1002/2014JD022787>, 2015.
- Wallin, G., Hall, M., Slaney, M., Räntfors, M., Medhurst, J., and Linder, S.: Spring photosynthetic recovery of boreal Norway spruce under
850 conditions of elevated [CO₂] and air temperature, *Tree Physiol.*, 33, <https://doi.org/10.1093/treephys/tpt066>, 2013.
- Wespes, C., Hurtmans, D., Clerbaux, C., Boynard, A., and Coheur, P.-F.: Decrease in tropospheric O₃ levels in the Northern Hemisphere observed by IASI, *Atmospheric Chemistry and Physics*, 18, 6867–6885, <https://doi.org/10.5194/acp-18-6867-2018>, 2018.
- WHO - World Health Organization: Health risks of ozone from long-range transboundary air pollution, 2008.
- Wittig, V. E., Ainsworth, E. A., Naidu, S. L., Karnosky, D. F., and Long, S. P.: Quantifying the impact of current and future tropo-
855 spheric ozone on tree biomass, growth, physiology and biochemistry: a quantitative meta-analysis, *Glob. Change Biol.*, 15, 396–424, <https://doi.org/10.1111/j.1365-2486.2008.01774.x>, 2009.
- WMO: Guide to Instruments and Methods of Observation: 2018, first published in 1950, ISBN: 978-92-63-10008-5, 2018.
- Young, P. J., Archibald, A. T., Bowman, K. W., Lamarque, J.-F., Naik, V., Stevenson, D. S., Tilmes, S., Voulgarakis, A., Wild, O., Bergmann,
860 D., Cameron-Smith, P., Cionni, I., Collins, W. J., Dalsøren, S. B., Doherty, R. M., Eyring, V., Faluvegi, G., Horowitz, L. W., Josse, B., Lee, Y. H., MacKenzie, I. A., Nagashima, T., Plummer, D. A., Righi, M., Rumbold, S. T., Skeie, R. B., Shindell, D. T., Strode, S. A., Sudo, K., Szopa, S., and Zeng, G.: Pre-industrial to end 21st century projections of tropospheric ozone from the Atmospheric Chemistry and Climate Model Intercomparison Project (ACCMIP), *Atmos. Chem. Phys.*, 13, 2063–2090, <https://doi.org/10.5194/acp-13-2063-2013>, 2013.

Supplement

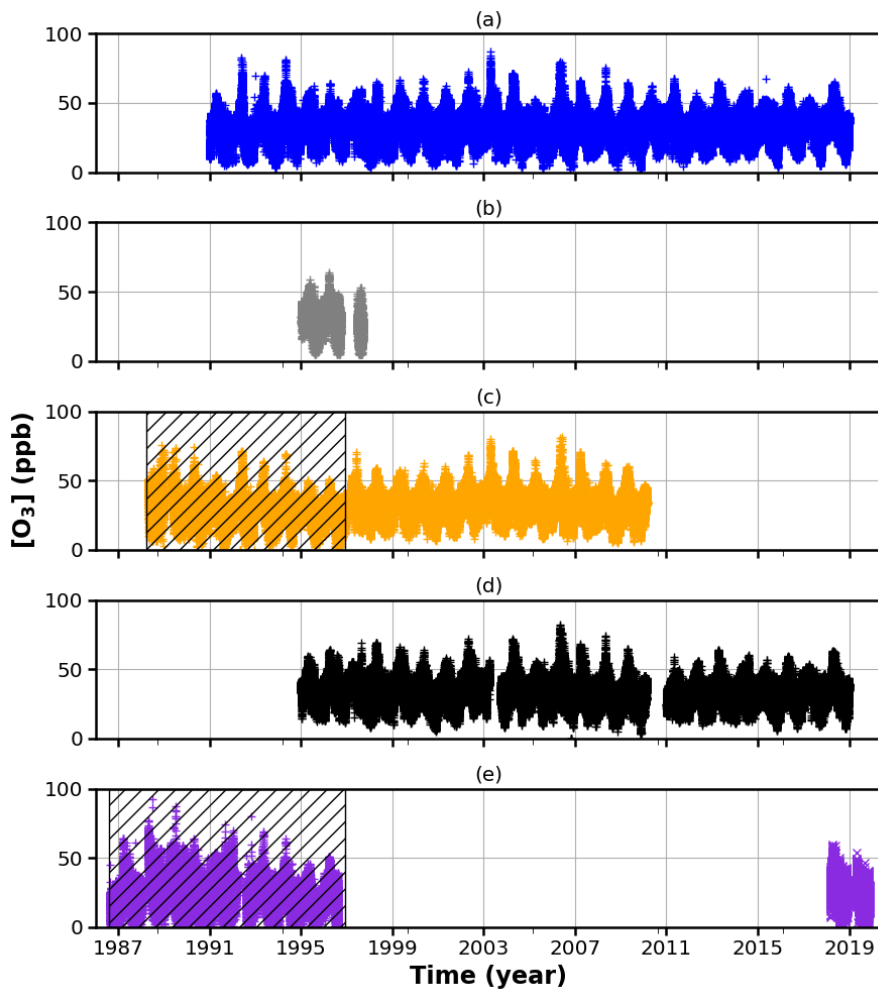


Figure S1. Time series of ozone observations in northern Fennoscandia (Tab. 1) (1986–2019). Data from EBAS until December 2018. The hatched areas indicate periods with insufficient quality control according to Solberg (2003). (a) Esrange (SWE); (b) Janiskoski (RUS); (c) Jergul/Karasjok (NOR); (d) Pallas (FIN); (e) Svanvik (NOR).

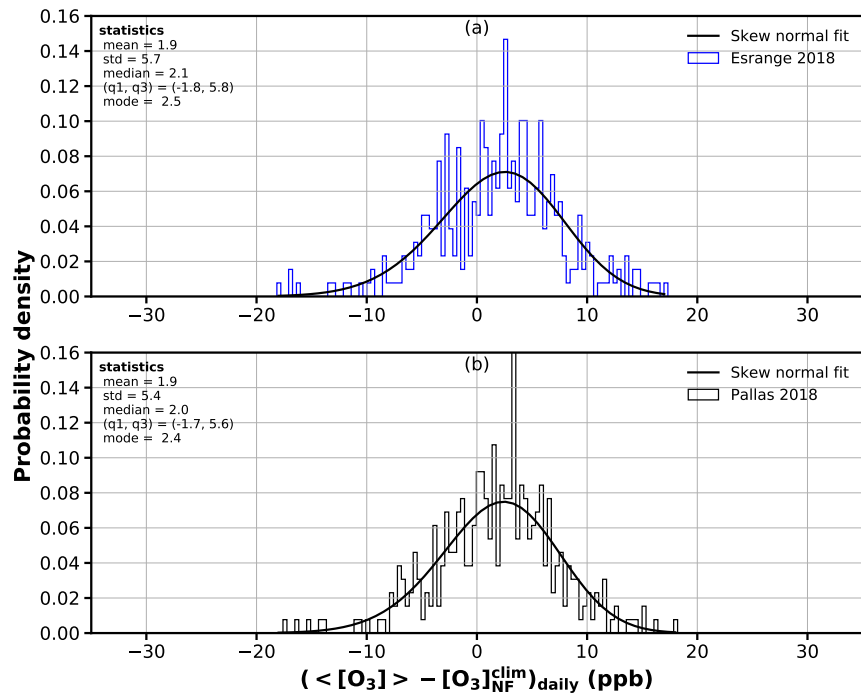


Figure S2. Probability density functions of ozone concentration residuals. 2018 with respect to respective climatology for different sites in Fennoscandia. (a) Esrange; (b) Pallas.

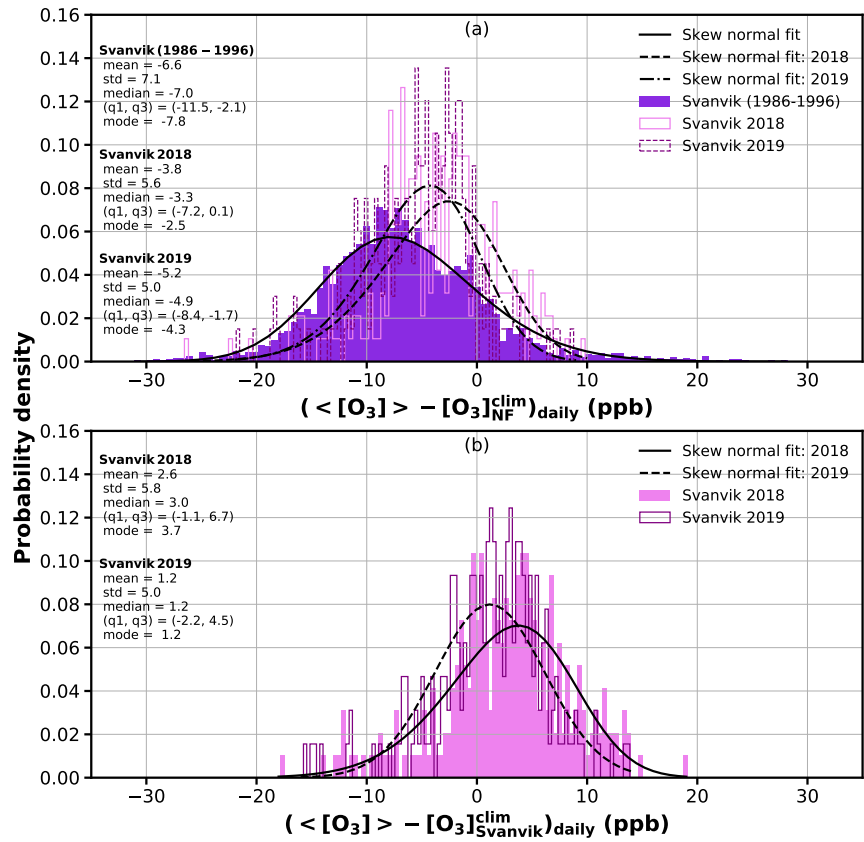


Figure S3. Probability density functions of ozone concentration residuals. 2018/19 observations at Svanhovd with respect to derived climatologies for (a) Northern Fennoscandia; (b) Svanvik.

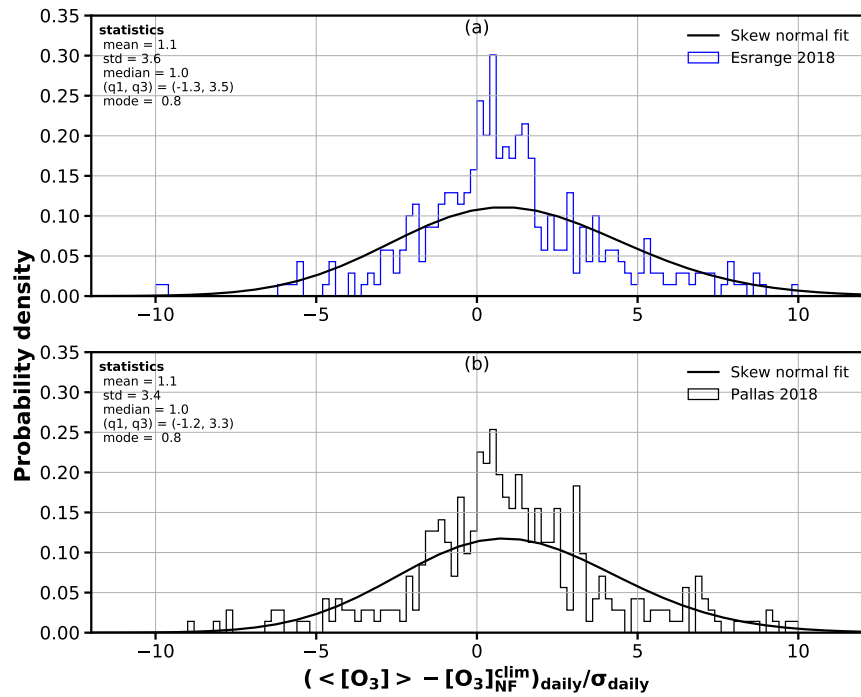


Figure S4. Student's t-test assuming same sample uncertainty in both, climatology and 2018 observations for different sites in Fennoscandia. $\Delta[O_3]$ in Fig. S2 are significantly different from zero-hypothesis on the 1σ level. (a) Esrange; (b) Pallas.

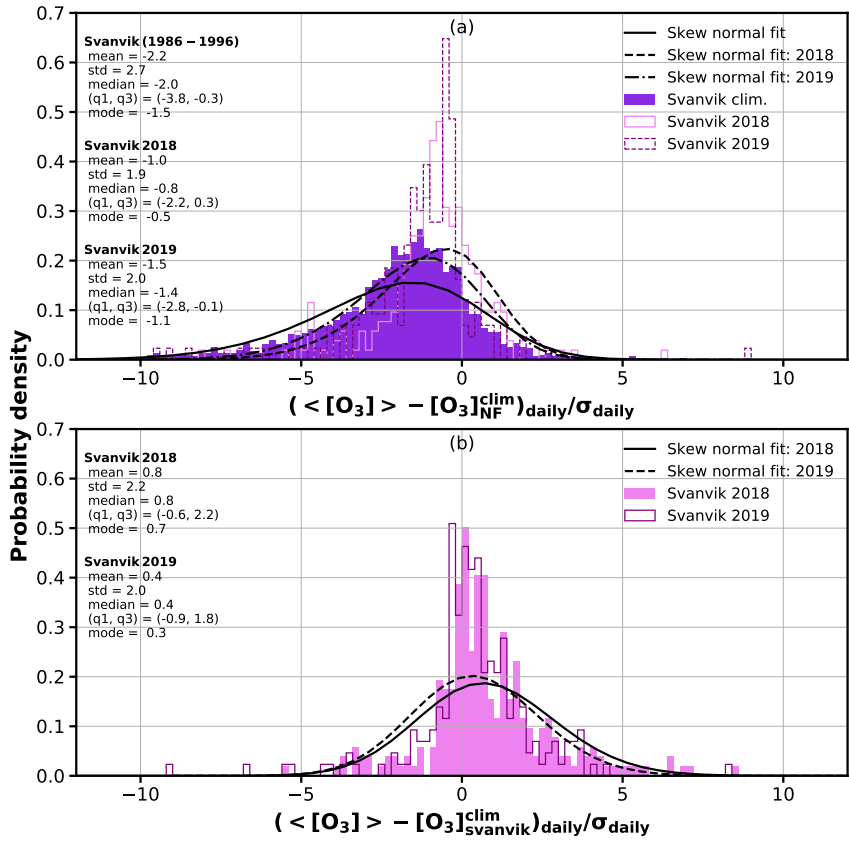


Figure S5. Student's t-test assuming same sample uncertainty in both, climatology and 2018/19 observations at Svanhovd with respect to derived climatologies for (a) Northern Fennoscandia; (b) Svanvik. $\Delta[\text{O}_3]$ in Fig. S2a) are significantly different from zero-hypothesis on the 2σ , 1σ level, respectively. $\Delta[\text{O}_3]$ in Fig. S2b) are not significantly different from zero-hypothesis.

Table S1. Mapping manual parameters used in DO3SE modeling of Boreal species. Values in brackets represent required “dummy” values. A “-” means that this parameter is not required for this species. The T_{\max} value is set at 100 °C to simulate the weak response to high temperatures of Norway spruce and birch trees growing under Northern European conditions (stomatal response is instead mediated by high VPD values).

Parameter	Land cover (POD ₁ SPEC)		
	Norway Spruce	Birch	Grassland
Land cover type (Tree) species	Coniferous	Broadleaf deciduous	Perennial grasslands
Norway spruce		Silver birch	
g_{\max}	125	240	190
f_{\min}	0.1	0.1	0.1
light_a	0.006	0.004	0.011
T_{\min}	0	5	10
T_{opt}	20	20	24
T_{\max}	100	100	36
VPD _{max}	0.8	0.5	1.75
VPD _{min}	2.8	2.7	4.5
$\Sigma \text{VPD}_{\text{crit}}$	(1000)	(1000)	(1000)
PAW _t	-	-	-
SWP _{max}	-0.5	-0.5	-0.1
SWP _{min}	-1.5	-1.5	-1
f_{O_3}	-	-	-
$A_{\text{start-FD}}$	1	100	1
$A_{\text{end-FD}}$	365	307	365
Time window length			
Leaf dimension (cm)	1	5	2 *
Canopy height (m)	20	20	0.2
$f_{\text{phen a}}$	0.0	0.0	1
$f_{\text{phen b}}$	(1.0)	(1.0)	1
$f_{\text{phen c}}$	1.0	1.0	1
$f_{\text{phen d}}$	(1.0)	(1.0)	1
$f_{\text{phen e}}$	0.0	0.0	1
$f_{\text{phen 1 FD}}$	20	20	(0.0)
$f_{\text{phen 2 FD}}$	(0.0)	(0.0)	(0.0)
$f_{\text{phen 3 FD}}$	(0.0)	(0.0)	(0.0)
$f_{\text{phen 4 FD}}$	30	30	(0.0)
LIM _{start FD}	(0.0)	(0.0)	(0.0)
LIM _{end FD}	(0.0)	(0.0)	(0.0)
LAI _{min}	5	0	2
LAI _{max}	5	4	3.5
L _s	1	20	140
L _E	1	30	135

* Not given, set to match wheat (grass species) and potato (forb species, including legumes).

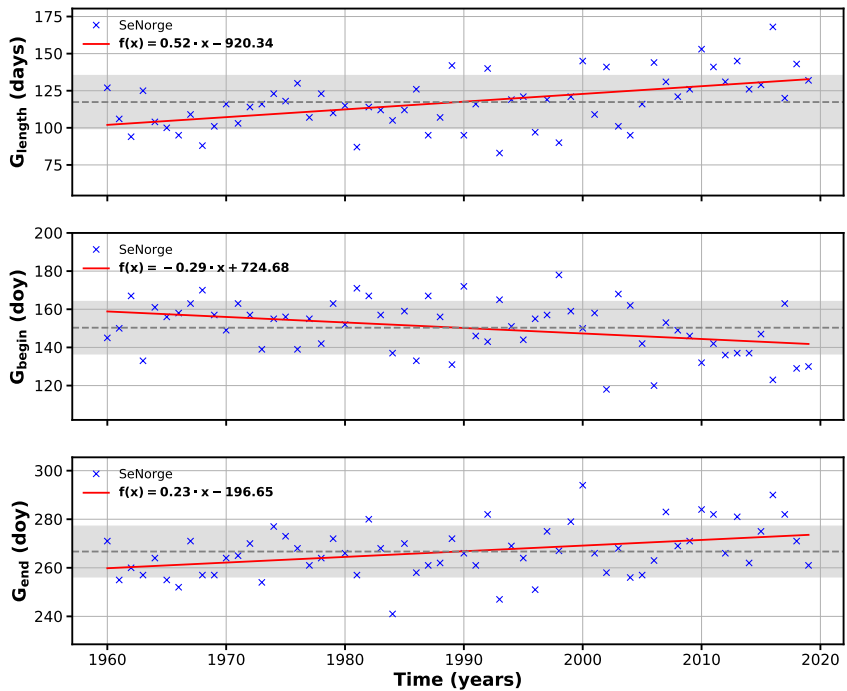


Figure S6. Estimated shift and prolongation of growing season at Svanhovd over the past 6 decades based on data from NVE, Meteorologisk Institutt, Kartverket (2020).